1-1-2010

Nondestructive Evaluation Of A Polymer Composite Hip Implant Using Lock-In Thermography

Ehsan Rahim
Ryerson University

NONDESTRUCTIVE EVALUATION OF A POLYMER COMPOSITE HIP IMPLANT USING LOCK-IN THERMOGRAPHY

by

Ehsan Rahim
B.E. (Mechanical Engineering)
N.E.D. University of Engineering and Technology, Karachi, Pakistan

A Thesis
presented to Ryerson University
in partial fulfilment of the
requirements for the
Degree of Master of Applied Science
in the Program of
Mechanical Engineering

Toronto, Ontario, Canada, 2010

Author's Declaration

I hereby declare that I am the sole author of this thesis.

I authorise Ryerson University to lend this thesis to other institutions of individuals for the purpose of scholarly research.

I further authorise Ryerson University to reproduce this thesis by photocopying or by other means, in total or in part, at the request of other institutions or individuals for the purpose of scholarly research.

Abstract

NONDESTRUCTIVE EVALUATION OF A POLYMER COMPOSITE HIP IMPLANT USING LOCK-IN THERMOGRAPHY

Ehsan ur Rahim

Masters of Applied Science

Department of Mechanical & Industrial Engineering

Ryerson University, Toronto, Ontario, Canada, 2010

Lock-in thermography, combined with finite element analysis and experimental testing, was used to investigate the stress/strain pattern in a novel composite hip implant made of carbon fibre and polyamide 12 (CF/PA12). In this study, the geometry of the hip implant was first modelled and analysed in ANSYS workbench 11. Different virtual loads of 800N, 1400N and 2200N were applied on the finite element model of the hip stem at an adduction angle of 15°, thereby replicating the present experimental setup. The values of strains obtained were confirmed by replicating the experiment by using stain gauges. A Pearson's correlation (R^2=0.98) was obtained, which indicated good agreement between the FEA model and experimental hip stem. The hip implant was again subjected to similar loading conditions, and stresses were recorded by using a thermal camera at corresponding vertices. The comparison of results showed good agreement between the values of stress calculated from the strain gauge experiment and stress obtained from thermography. This study showed that it was possible to find stresses in a hip implant reliably by thermography.

Acknowledgements

The writing of my graduate studies thesis would not have been possible without the overwhelming support and understanding of my professors, colleagues and friends.

First and foremost, I would like to express my sincere thanks to my supervisor, Dr. Habiba Bougherara, for her overwhelming support, encouragement and understanding. Her wisdom and rigorous guidance throughout my graduate studies are highly appreciated.

Thanks to Dr. Rad Zdero, my co-supervisor, for his expert advice on experimental biomechanics and for the use of the Martin Orthopaedic Biomechanics Laboratory at St. Michael's Hospital, Toronto.

Thanks to Mr. Suraj Shah for his expert advice and valuable technical assistance in the fields of infrared thermography and strain gauge experimental work. His time and assistance were crucial to the completion of my thesis in a timely manner.

Ms. Leah Rogan and the School of Graduate Studies at Ryerson University, for their assistance throughout the course of my graduate studies.

I would also like to extend my gratitude to my best friend, Lubna Khan, for the unyielding support and patience she offered me during the writing of this thesis.

Finally, it is a pleasure to acknowledge the very considerable help of my wife, Dr. Sana Ehsan, M.D., at every step of my educational endeavours. From the beginning, she allowed me considerable time away from the family pursuing my educational and research activities and supported me in good times and more usually, in bad times.

This page is intentionally left blank.

Table of Contents

List of Figures

List of Tables

Medical Terminology Used

Abduction	outward movement, away from the median axis of the body
Adduction	inward movement, towards the median axis of the body
Arthritis	acute or chronic inflammation of a joint, often accompanied by pain and structural changes and having diverse causes, as infection, crystal deposition, or injury
Arthroplasty	the surgical repair of a joint or the fashioning of a movable joint, using the patient's own tissue or an artificial replacement
Articular	of or related to the joints
Biomimetic	imitating biology and/or living tissue
Calcar	is the name given to a spur of cartilage arising from inner side of ankle and running along part of outer interfemoral membrane
Cancellous Bone	spongy bone tissue
Cortical Bone	hard, compact bone tissue
CT or CAT	computer tomography or computed axial tomography; an X-ray technique for producing cross-sectional image of the body
Diaphysis	central section of a long bone, between the growth areas at each end.
Distal	situated away from the point of origin or attachment, as of a limb or bone; terminal
Femur	thighbone; a bone in the human leg extending from the pelvis to the knee, that is the longest, largest, and strongest in the body
Lateral	direction away from the midline of the body or the sagittal plane
Medial	inward direction towards the midline of the body
Osseointegration	is the direct structural and functional connection between living bone and the surface of a load-bearing artificial implant
Osteoarthritis	the most common form of arthritis, usually occurring after middle age, marked by chronic breakdown of cartilage in the joints leading to pain, stiffness, and swelling.
Osteolysis	dissolution or degeneration of bone tissue through disease

Osteoporosis	increase in bone porosity and subsequent decrease in bone density through disease; usually occurs after osteopenia
Physiologic	relating to the way that living things function, rather than to their shape or structure
Prosthesis	an implant; a device, either external or implanted, that substitutes for or supplements a missing or defective part of the body
Proximal	situated toward the point of origin or attachment, as of a limb or bone
Resorption	dissolution or removal of a substance, e.g. bone tissue
Synovial	belonging to, or related to, the synovial joint or diarthrosis

Nomenclature

E	Elastic modulus / Modulus of elasticity / Young's modulus
N	Newton
Pa	Pascal
Q	Heat flux
t	Thickness
k	Thermal conductivity
A_h	Surface area on which the energy is incident
L	Length
W	Width
T	Temperature
Φ	Phase value
S	Signal value
α	Coefficient of thermal expansion
C_p	Specific heat capacity
σ	Stress
με	Microstrain ($\varepsilon \times 10^{-6}$)
ε	Strain
ν	Poisson's ratio
ρ	Density

Chapter 1 . INTRODUCTION

1.1 Background

As human life expectancy continues to increase, the number of people undergoing joint replacement surgery, e.g., total hip and knee replacement, is also increasing considerably [1].

The younger generation is more concerned with games and physical activities than the elderly population, thus imposing larger and more frequent loads on the joint leading to joint failure [2, 3]. Due to this demographic characteristic of patients who undergo hip arthroplasty, the durability and the longevity of the prosthesis is a challenge [4, 5].

Many patients with high levels of immobility and pain may opt to undergo major joint replacement surgery relieving them of pain and restoring their physical independence [6]. It is a common and highly successful method of treatment to replace a diseased hip with an artificial joint. It must be taken under consideration that the implant provides long-term fixation and does not need to be replaced prematurely in order to reduce trauma and the social cost to the patient. It is necessary to lessen the possibility of this happening to a minimum [7, 8].

Surgically, both the femoral and acetabular bearing surfaces are replaced with metallic, polymeric, and/or ceramic components during total hip arthroplasty. Since the last century, research work has been undergoing on different combinations of materials to find an appropriate candidate for total hip arthroplasty [9].

Biomaterials are those materials which are compatible with living tissue. These materials are used to direct, enhance or substitute functions of living tissues of the human body and can be either natural or artificial [10].

The phenomenon of using artificial biomaterial is not new, as artificial eyes, ears, teeth and noses have been found on ancient Egyptian mummies. Waxes, glues and tissues were used to recreate missing or flawed parts of the body by Indians and Chinese. The continuous improvement in synthetic materials, surgical techniques and sterilization methods over the centuries allowed the use of biomaterials in different ways.

In medical practice today, biomaterials are used in the form of implants (bone plates, joint replacements, heart valves, intraocular lenses, dental implants etc.) and medical devices (pacemakers, blood tubes etc.). These implants and devices help in restoring the function of traumatized or degenerated tissues or organs, to aid in curing, to improve function, and to correct abnormalities, thus improve the quality of life of the patients [11].

Orthopaedic pioneering researchers and surgeons have encouraged materials scientists and engineers for many years to develop implants and devices to cure diseases and injuries involving the skeleton. The surgical technique to relieve the pain and to restore the function by creating an artificial joint is known as arthroplasty.

The biocompatibility and low rigidity of carbon fibre reinforced composite is comparable to that of cortical bone, which makes it a candidate material for use in orthopaedic applications. For total hip replacement and internal fixation, Christel *et al.* suggested these composites and polymers as candidate biomaterials [12, 13].

The primary objective in cementless joint replacement surgery is fast osseointegration of bone prostheses and long-term fixation. The physical, mechanical, or chemical properties of the ideal joint replacement implant must match those of the host tissue for optimal osseointegration. Scientists and engineers design robust and stiff implants for femoral components. They must keep in mind that it will be subjected to millions of load cycles per year with load averaging four times the body weight and lasting for 15 to 20 years.

Studies have shown that there is a difference between the stiffness of a proximal femur and high stiffness implant, which results in the loss of proximal cortical bone stock. This phenomenon of bone loss adjacent to an implant is known as ‘‘stress shielding’’ which occurs due to a stiff implant fixed distally. It is believed that the load transfer to the bone tissue through the implant surfaces may be significantly different from the load originally applied on the same region before implantation. In this situation, load is reduced in the proximal femur which subsequently leads to bone resorption and implant loosening [14].

One of the leading causes of chronic disability is osteoarthritis (OA). It has been estimated that symptomatic knee OA occurs in 13% of persons aged 60 years and above. As the population

ages this percentage is expected to rise. OA results are measured in many ways including patient-relevant measures (measures of pain and function), structural measures (such as plain radiographs and magnetic resonance imaging), and biomarkers in the form of molecules or molecular fragments that are released as a result of joint tissue metabolism [15].

About 50–80% of the elderly population suffers from OA, and community-dwelling older adults are unable to perform daily living activities due to arthritis. Daily activities such as walking, climbing stairs and using the bathroom can be severely compromised because of the arthritis of the knee or hip. OA is treated by exercise therapy, pharmacologic therapy, patient education and surgical procedures [16]. The reasons for OA are complex, including genetics, biochemistry and biomechanics. Biomechanical factors are the main cause of OA, and any hidden biomechanical abnormality should be investigated for the conservative management of the disease [17].

1.2 Statistical Analysis of Hip Replacements in Canada

The Canadian Joint Replacement Registry (CJRR) is an organization managed by the Canadian Institute of Health Information (CIHI) from where all the data have been obtained. Data for the fiscal year 2008-2009 are the most recent Canadian data available.

There were 62,169 hospitalizations for hip and knee replacements in Canada on Canadian residents in 2006–2007 as shown in **Error! Reference source not found.**. Since 1996-1997, there has been a significant 10-year increase of 101% from only 31,043 to 62,196 as well as a one-year increase of 6% from only 58,470 procedures in 2005-2006. In the year 2005-2006, there was 12.5% increase in the number of procedures for hip replacement than it was a year earlier in the fiscal year 2004-2005.

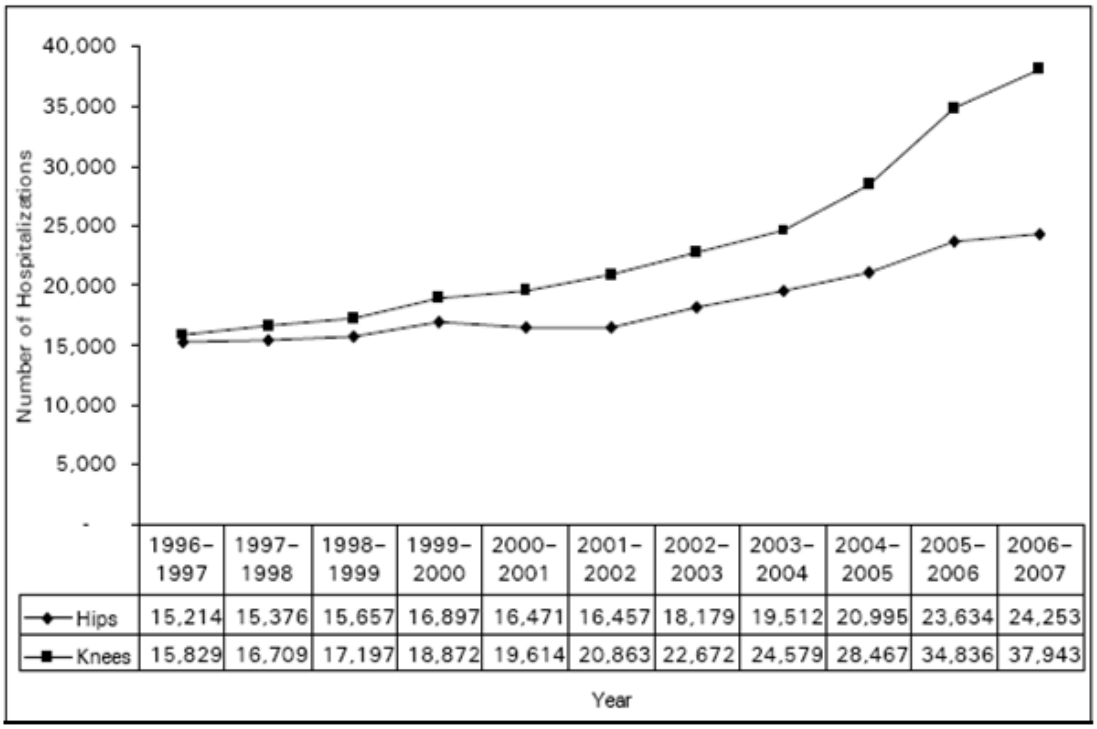

	1996–1997	1997–1998	1998–1999	1999–2000	2000–2001	2001–2002	2002–2003	2003–2004	2004–2005	2005–2006	2006–2007
Hips	15,214	15,376	15,657	16,897	16,471	16,457	18,179	19,512	20,995	23,634	24,253
Knees	15,829	16,709	17,197	18,872	19,614	20,863	22,672	24,579	28,467	34,836	37,943

Figure 1-1 Number of hospitalizations for hip and knee replacement procedures in Canada [18]

Primary and revision surgeries have generally increased since 1996-1997. In the year 2005-2006, the number of hospitalizations for hip replacements was 23,634. In the year 2006–2007 there were total 62,196 hospitalizations for hip (24,253) and knee (37,943) replacements performed across Canada; the majority of Canadians were 65 years or older (63% for hip and 64% for knee). Given these numbers, it is apparent that the social and economic cost of hip disease and replacement, in Canada alone, is a primary motivator for orthopaedic biomechanics research.

1.3 Current Study: Research Question and Goals

This study is conducted to assess the validity of a nondestructive testing technique, i.e., infrared thermography, for use in evaluating total joint replacements. Specifically, a composite hip implant made of carbon fibre reinforced polyamide-12 (CF/PA12), with properties comparable to cortical bone tissue, is used to conduct experimental and numerical analysis to measure the strain/stress that is generated. The results obtained from these two experimental and numerical models are then compared with the results obtained from lock-in thermography. As this

composite material matches the properties of a cortical bone, it may prevent loosening of the hip implant due to stress shielding, which is a main cause for revision surgery for hip implant patients. The main question that the present study will address is: *Can the stress/strain results from lock-in thermography and finite element analysis be validated by experimental testing (strain gauges) on a composite CF/PA12 hip implant?*

The distinct goals of this study are: 1) To carry out an experimental study on a composite hip implant system using strain gauges and IR thermography utilizing loads within the elastic region to avoid permanent damage to the implant; 2) To develop a 3D model of the hip implant system using Solid Works and evaluate it using finite element analysis; 3) To compare all three techniques mentioned above against each other with respect to strain and/or stress.

1.4 Current Thesis Outline

This thesis is divided into 6 main chapters. The statistics of primary orthopaedic replacements carried out in Canada and the research question and goals of this study are explained in Chapter 1. Total hip arthroplasty, prosthetic hip implants and their failures, a brief introduction of polymer composites as a candidate material, and the principle of IR thermography are described in Chapter 2. Chapter 3 describes the experimental setup for IR thermography with a brief description of the thermal camera used in this study. The use of strain gauges and their selection and installation on the hip implant, the mechanical testing procedure, the geometric modelling of the hip implant used to develop the finite element model, and the finite element analysis conducted for the implant are also delineated in this chapter. The results from finite element analysis, strain gauge experiments and infrared thermography are compiled in Chapter 4. Chapter 5 of this thesis discusses the results obtained in present study and those from previous studies. Limitations and future work possible are also given. Chapter 6 is the last chapter of this study which states conclusions. Appendices and references are given at the end of this thesis.

Chapter 2 . LITERATURE REVIEW

2.1 Total Hip Arthroplasty

2.1.1 Background

The most flourishing intervention in orthopaedics is without doubt the total hip replacement (THR) used in the surgical procedure known as total hip arthroplasty (THA) [19]. When it comes to patient satisfaction, pain reduction, functional improvement and the absence of further surgery of more than 90% at a minimum 10-year follow-up evaluation, several continued follow-up studies have reported good clinical success rates in THA [20, 21]. Therefore THRs are largely acknowledged as successful devices used in surgical arthroplasty procedures to improve chronic joint pain and enhance functional ability [22].

The discovery and use of ultra-high molecular weight polyethylene (UHMWPE) as a bearing surface for the acetabular component added an extra boost to the success of THA in the second half of the 20th century [22].

THA is an orthopaedic procedure involving surgical excision of the head and proximal neck of the femur and exclusion of acetabular cartilage and subchondral bone. In this procedure an artificial canal is created in the proximal medullary area of the femur and a metal femoral prosthesis, composed of a stem and small-diameter head, is inserted into the femoral medullary canal [23] as shown in Figure 2-1

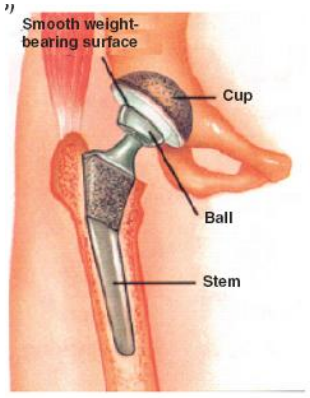

Figure 2-1 Schematic of a prosthetic device in total hip arthroplasty (THA) [24]**.**

More than 55,000 hip replacement procedures are performed annually in the UK alone, and this number is expected to increase [25]. Due to effective results, the hip prosthesis has been the most active area of joint replacement research and development for decades. Arthroplasty devices for hip joint have been in progress since the early 1900s.

A major improvement in the effectiveness of hip implants was made around 1960 by Charnley, who introduced a THA device made of a metal femoral prosthesis connected to bone with polymethyl methacrylate (PMMA), and an acetabular part made of UHMWPE, also attached to bone with PMMA [26]. PMMA bone cement remains the most familiar mode of attachment of the femoral component in THA, since it was introduced by Charnley 50 years ago [27].

2.1.2 Indications for the Replacement of Hip Joints

THA is usually suggested after failure of nonsurgical treatment and is generally performed in patients with severe joint disease. Moreover, racial, socioeconomic and sex differences in the rates of THA have been recognized. There are several reasons that are anticipated to explain this variation, such as differences in health care systems, population demographics, frequency of the disease, access to surgery, population awareness about THA, and/or willingness to consider THA. Lastly, another reason for the disparities is the variability of orthopaedic surgeons' opinions about the suitable time to perform surgery, and/or the availability of appropriate patients to undergo the operation [28].

The use of THA is still a growing trend in developed countries; however, surgical rates vary moderately across regions of countries such as the United States and elsewhere, a finding not explained mainly due to the differences in the prevalence of hip disease. Variations in clinical decision making may also account for this. Inexplicable variations in surgery rates, identification of inappropriate care, and ever-increasing health care costs raise questions about potential underuse or overuse of many medical and surgical procedures, including orthopedic procedures [29, 30].

The most suitable candidate for THA is a young patient who is suffering from persistent medical symptoms and pain that has failed to be addressed by most of the conservative methods of treatment. A reasonable course of treatment comprises of cessation of irritating activities,

nonsteroidal anti-inflammatories, and a course of physical therapy that focuses on hip flexor and anterior hip capsule stretching [31].

THA is a recommended option for almost all those patients who are suffering from diseases of the hip that cause chronic discomfort and/or significant functional impairment. At a National Institute of Health sponsored workshop, the following statement was issued: ‘‘NIH Consensus Statement concluded that candidates for THA should have moderate to severe persistent pain, disability, or both, not substantially relieved by an extended course of non-surgical management in association with radiographic signs of OA” [32].

2.1.3 Reasons for Prosthesis Failure

The huge majority of total hip replacements currently implanted are comprised of a hard metal or ceramic femoral head articulating against an UHMWPE acetabular cup. Over the last decade, evidence has gathered to indicate that these implants are prone to failure largely due to late aseptic loosening, and few tend to survive after 25 years [33].

Fragments that results from damage to the surface of polyethylene components of total joint replacements has formerly been shown to give way to long-term problems such as loosening and infection. Surface damage has been linked with fatigue processes due to stresses arising from contact between the metal and polyethylene components in these implants [34].

It is documented quite extensively that widespread wear takes place at articular surfaces in total joint replacements *in vivo*. This is so irrespective of whether one or both of the bearing components are made of UHMWPE, a ceramic, or a metal. It has often been suggested that this wear is associated with the stress at the contacting surfaces [35] .

UHMWPE has been the most extensively used bearing surface in total hip and total knee replacements. However, in recent years it has been acknowledged that the wear of the UHMWPE may be the limiting factor for the long-term success of prostheses [36].

2.1.4 The Need for Polymer Composites for Orthopaedic Implants

Over the last few decades, research and engineering efforts have been moving from traditional monolithic materials to fibre reinforced polymer-based materials. This is mainly because of the

unique advantages of their high strength-to-weight ratio, their non-corrosive properties, and their high fracture toughness. These composite materials are made of high strength fibres, such as carbon, glass, and aramid, and a low strength polymeric matrix [37]. Efforts continue to focus on the development of a "conservative" implant that could replace the femoral side of a total hip arthroplasty. Such an implant favours physiologic bone remodeling. Proximally fixed femoral components that are inserted without the use of cement to achieve these goals have been used in a number of design concepts around the world [38].

Most of the composites aim at an improvement and perfection of mechanical properties such as stiffness and strength [39]. The use of composite materials in orthopaedic surgery paves the way for a variety of new implant designs. Exceptional mechanical properties; namely, radiolucency, biocompatibility and low weight are the major benefits when compared with metals in clinical use today [40].

Campbell *et al.* performed two studies using a novel composite made from carbon fibres and polyamide (CF/PA12). The first study dealt with the manufacturing and properties of CF/PA12 hollow cylinders and hip implant femoral stems, while the other investigated the performance of the femoral stems [41, 42]. They assessed the optimal manufacturing conditions for CF/PA12 in order to attain a composite structure with the best consolidation quality possible and therefore the maximum stiffness and rigidity. Actual femoral hip implants were manufactured with CF/PA12 in the form of braided sleeves of co-mingled CF and PA12 strands. The femoral implants were made by inflatable bladder moulding, where six layers of braided sleeves of CF/PA12 yarns were placed around a silicone bladder mandrel [41, 42] as shown in Figure 2-2.

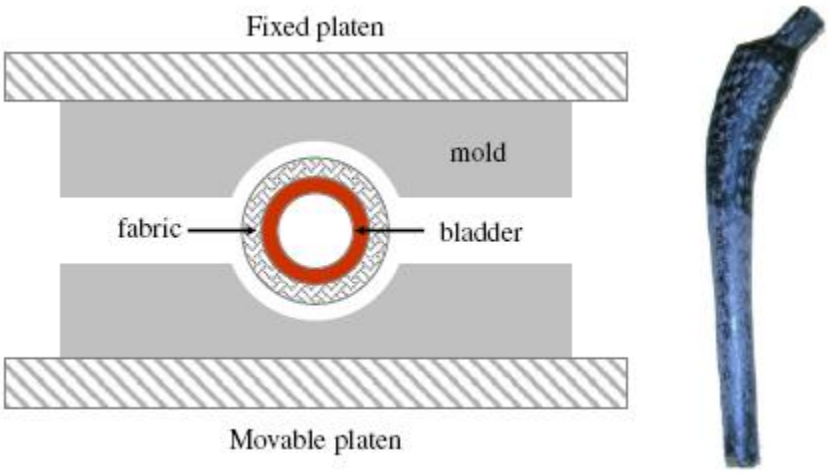

Figure 2-2 Mould used in inflatable bladder molding and resulting composite femoral stem [42]

Campbell *et al*. studied a number manufacturing conditions and found that optimal moulding conditions could be achieved at a temperature of 250°C and a compression pressure of 480 kPa, with a holding time of 5 minutes. A comparison was made between the compression performance of femoral stems manufactured at different moulding conditions. The stress-strain curves revealed that the femoral implants tended to experience linear stress-strain behaviour when subjected to compression, followed by yielding and sudden softening until an area of stability was reached. Their results were the same as those of previous studies [43-45]. Yielding took place by shear deformation at $\pm 45^{o}$ with respect to the loading axis, i.e., along the direction of the carbon fibres. At failure, the maximum load (28-32 kN) was reported to be approximately 10 times greater than normal physiological loads experienced during gait (2.5-3 kN) [41, 42].

In their second published study, Campbell *et al.*'s experiments were performed on two specimens made of CF/PA12; a hollow cylinder and a femoral hip implant. The composite was tested for fatigue performance, and it was found that the CF/PA12 hip implant surpassed the required fatigue performance [41, 42].

Hollow cylinders of CF/PA12 (22 mm outer diameter, 3 mm wall thickness) were subjected to compressive and flexural (short-term) tests, while cyclic fatigue (long-term) tests were performed on both cylindrical specimens as well as on actual femoral implant geometry. When a maximum load of 28.6 kN was applied, the compression tests indicated a modulus of 12.2 GPa

and an ultimate strength of 155 MPa. These values were almost identical to cortical bone tissue values of 11.5-17 GPa and 133-193 MPa, respectively, as shown in Table 2-1. The flexural modulus and ultimate strength of the CF/PA12 cylinder were measured as 16.4 GPa and 180 MPa respectively which was also within close range of cortical bone tissue properties of 14.3-21.1 GPa and 178-250 MPa, respectively [46]. The comparison between CF/PA12 cylinders and cortical tissue when subjected to compression is given Table 2-1. The bending stiffness calculated was based on the product of the elastic modulus and moment of inertia. The bending stiffness of the composite cylinders (22 mm outer diameter) was 180-425 N-m^2, which was within the acceptable range of the cortical bone (with outer cortex diameter of 25-30 mm) bending stiffness of 170-500 N-m^2 [47].

Specimen Material	Maximum Compressive Load (kN)	Elasticity Modulus (GPa)	Ultimate Strength (MPa)
CF/PA12 [41, 48]	28.6 ± 3.8	12.2 ± 1.3	155 ± 27
Cortical Bone [49]	-	11.5-17	133-193

Table 2-1 Compression test results of CF/PA12 cylinders compared to cortical tissue

The cyclic fatigue tests showed that the CF/PA12 cylinders failed at 10^6 cycles at a maximum fatigue stress of 101 MPa (load of 17 kN) and at 10^7 cycles for 95 MPa (18 kN). These results indicate fatigue limits of 10^6 or more for loads that are at least 6 times more than the 3000 N recommended by ASTM standards for hip arthroplasty femoral components. These results provide realistic evidence that CF/PA12 is an exceptional choice of material for orthopaedic applications in general [41, 42]. The main factors involved in the selection of a biomimetic material are given in Table 2-2.

Factors	Description		
	Chemical/Biological characteristics	**Physical characteristics**	**Mechanical/Structural characteristics**
1st Level material properties	• Chemical composition (bulk & surface)	• Density	• Elastic modulus • Shear modulus • Poisson's ratio • Yield strength • Compressive strength
2nd Level material properties	• Adhesion	• Surface topology • Texture • Roughness	• Hardness • Flexural modulus • Flexural strength
Specific functional requirements (based on applications)	• Biofunctionality • Bioinert • Bioactive • Biostability • Biodegradation behaviour	• Form & geometry • Coefficient of thermal expansion • Electrical conductivity • Colour aesthetics • Refractive index • Opacity or translucency	• Stiffness or rigidity • Fracture toughness • Fatigue strength • Creep resistance • Friction & wear resistance • Adhesion strength • Impact strength • Proof stress • Abrasion resistance
Processing & Fabrication	Reproducibility, quality, sterilizability, packaging, secondary process-ability		
Characteristics of host: tissue, organ, species, age, sex, race, health condition, activity, systemic response			
Medical/surgical procedure, period of application / usage			
Cost			

Table 2-2 Key factors for the selection of materials for biomedical applications[37]

2.2 Infrared Thermography

2.2.1 Introduction

The motivation for conducting thermal analysis during mechanical tests is to analyze a physical phenomenon of the specimen, to categorize and authenticate the thermodynamic framework of a macroscopic model, or to validate a hypothesis. The infrared images obtained with a thermal camera are used to identify a heat source field by analyzing the surface temperature [50].

Thermography has been a part of diagnosis in various medical fields. Its use in angiography [51-53], heart surgery [54, 55], and for prevention and early detection of breast cancer [56-63] is well established. IR thermography has been used to observe and measure the temperature gradient of bone [64-67] and dental implants [68, 69] when subjected to drilling. In aerospace engineering, lock-in thermography is widely used to detect the defects of composites [70-75]. Thermographic tests on composite materials for structural materials [76-81] and military applications [82, 83] have also been performed.

2.2.2 The Principle of IR Thermography

The principle of IR thermography when used as a nondestructive testing technique is that when heat travels through cracks, delaminations or other anomalies, the heat flow rate changes. Fourier's law describes the heat transfer by means of conduction within a material as well as from one material to another, which is described as:

$$Q = \frac{k.\Delta T}{t.A_h} \qquad \textbf{Equation 2.1}$$

where Q is heat flux, k is the thermal conductivity of material, A_h is the surface area on which the energy is incident, t is the thickness, and ΔT is temperature gradient [84]. The rate of conduction of heat is higher in materials with higher values of k, such as metals, than in an air gap (or vacuum) whose k value is nearly zero. The heat flow rate is dependent on the medium in which it is travelling and the presence of any anomalies in that medium. The thermal conductivity of fibre reinforced polymer composites is much lower compared to metals.

2.2.3 IR Thermography Techniques

IR thermography is effectively used for inspection of fibre reinforced polymer composites, insulation materials, composites bonded to metals, composite-concrete bonds, and flaws in concrete. As every material reacts differently to heat input, therefore, a variety of thermographic methods have been developed to suit individual material and geometric configurations. The energy sources can be broadly divided into distinct groups, namely, optical and mechanical. In optical excitation, the defects are stimulated externally, and energy is introduced to the surface of the test material until it reaches a flaw or discontinuity from where it is reflected back to the surface as thermal wave. When mechanical excitation heats the imperfections internally, mechanical fluctuations injected to the specimen pass through in multiple directions, dispersing energy at the discontinuities in the form of heat, which then travels to the surface by conduction.

Three typical methods of thermography based on these two excitation modes are lock-in thermography, pulsed thermography and vibrothermography.[85] The thermal excitation for the detection of flaws, cracks or damaged zones is generally performed by three methods, which belong to the category of externally applied thermal field (EATF). The principle of EATF thermography is that heat is applied to the specimen surface, and the radiation emitted from the surface, as a thermal gradient, is studied. The thermal gradient will be uniform, and the isotherms will be straight lines if there is no defect in the specimen. In case there is a defect in the specimen, the isotherms will be curved and a nonuniform temperature will be observed due to disturbance in the heat flow [86].

EATF thermography can be divided into active and passive, depending upon the mode of thermal excitation. In passive IR thermography, thermal excitation is done by an environmental source of heating (the sun). Passive thermography is generally used to inspect large objects such as an entire building whose thermal diffusivity can be effectively measured by using the sun as heat input. However, it is a qualitative mode of inspection [81].

Active thermography is a better option for defect detection due to its capability for quantitative measurement and classification of the defects. In this mode of thermal inspection, the specimen is energised by an incandescent light bulb, heat gun, flash lamp or quartz lamp. The intensity and duration of heat pulses from these sources are easily adjusted.

On the basis of the orientation of flaws and discontinuities in the specimen, EATF is further divided into parallel and normal modes [87]. Subsurface defects, such as delaminations, are effectively detected by the normal mode of EATF, as the infrared radiation emitted from the specimen surface may be interrupted due to the flaw and result in hot spots. The flaws of the surface, such as cracks, disturb the heat flow parallel to the specimen surface producing convexities in the isotherms or changes in surface temperature, which are efficiently detected by the parallel EATF mode. The ability to detect a flaw in the parallel mode is governed by the temperature difference across the crack and the duration for which the thermal pattern exists.

2.2.4 Lock-in Thermography

Introduction

One of the most widely used thermographic techniques is lock-in thermography, which is a nondestructive examination method that uses the phenomenon of thermal waves. A thermal wave is the reaction of a medium to an intermittent heat supply. Thermal waves are produced by intermittent heating of the surface of an object. These waves transmit into the solid object, and some of them are reflected back at the interfaces. The interfaces are the boundaries between dissimilar materials. A pattern of harmonic oscillating radiation is created when the incident and reflected thermal waves interfere on the surface of the specimen which can be recorded by instruments. The detection of the heat waves can be done by various means. Infrared thermography is one of the best and fastest methods for examination and defect detection of a large region in field test. Lock-in thermography is a combination of IR thermography and the thermal wave technique which allows for fast and remote nondestructive testing [88].

Principle of Lock-in Thermography

Lock-in thermography (LT), a quantitative technique, is used quite often for rapid and remote recognition of subsurface structures. In addition, depth quantification by LT is performed simply through the diffusion length equation. The principle of LT is established on the propagation and reflection of thermal waves that are initiated from the surface into the examined component by absorption of modulated radiation. Phase images are acquired by superposition of the initial thermal wave and its internal reflection which display hidden thermal structures down to a

certain depth below the surface. They are undisturbed by variation in emissivity of the surface and nonuniform distribution of heat emitted by the source [89].

In other words, in lock-in thermography, with adequate time for periodic heating, the surface temperature changes periodically in a sinusoidal pattern that develops from the transient state to the steady state. The heat source is used together with an adjusted intensity of a continuous sine wave source. The IR camera is utilized to detect the surface temperature of a thermal wave transmitting into materials and then produces a thermal image that displays the local variation of thermal waves in phase or amplitude [85].

Image Generation in Lock-in Thermography

The IR camera is an important component of lock-in thermography. The camera detects heat waves at the surface of the object and generates a two-dimensional thermal image depicting the temperature radiation on the surface. A phase image or an amplitude image can be generated by the phases and amplitudes of heat waves at the surface of the object. These images are helpful in indicating any variation in material properties and identifying subsurface structures.

Setup of Lock-in Thermography

The test specimen is exposed to sinusoidal thermal excitation, where input frequency controls its magnitude and phase during lock-in thermography. A modulated laser beam is used to thermally excite a specimen for a point inspection whereas heating is done by a modulated heating beam for a surface area inspection. An oscillating thermal field is generated inside the specimen due to this thermal excitation which is recorded by IR thermal camera from a distance. The setup is shown in Figure 2-3. The input and output signals are synchronized by a lock-in amplifier and thus the magnitude and the phase of the input and output heat waves can be calculated with respect to reference modulation. With the advancement in technology of IR thermography, the digitized data can be used to acquire the output signal in the absence of an amplifier. The local optical and infrared surface feature is related to the magnitude of the signal, and the phase is proportional to the transmission time delay. Due to the difference in the magnitude and phase of the signals between defective and defect free areas of the specimen, the subsurface flaws can be easily identified by monitoring the signals [90].

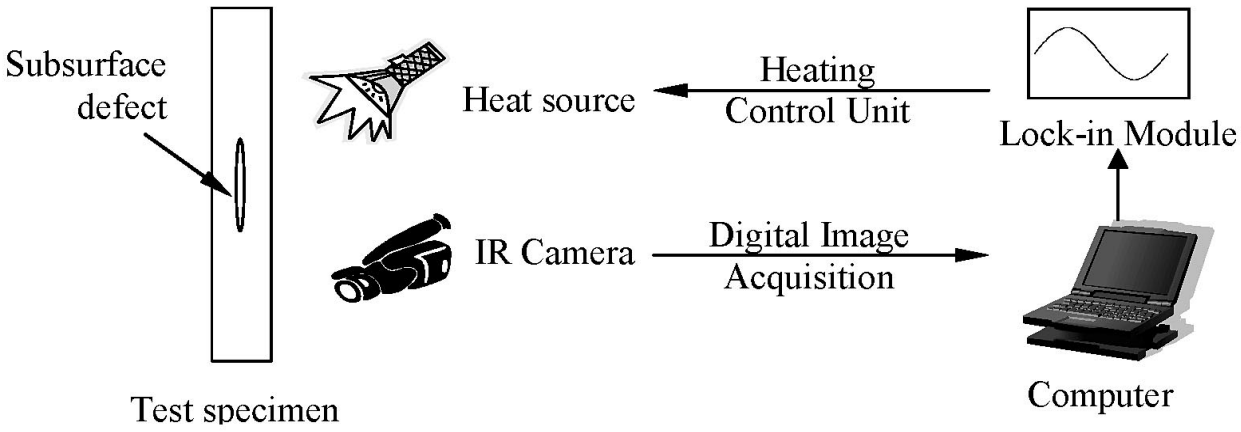

Figure 2-3 Typical of setup for lock-in thermographic inspection[84]

Advantages and Disadvantages of Lock-in Thermography

Lock-in thermography is used for defect detection near the surface, determining material properties and measuring the thicknesses of coatings. It is advantageous in the detection of delamination and is a flexible tool for nondestructive examination. Unlike x-rays, it is not harmful for humans and requires lesser time for examination. The lock-in thermographic technique is able to conduct nondestructive testing over a large region in a small interval of time. It is a noncontact technique, and the equipment is portable so that it can be used in almost any field test. It is also used in the inspection of printed circuit boards, electric installations and quality control in arc welding [91, 92].

Lock-in thermography has better depth resolution than pulse thermography [93]. It gives better results for slow thermal response materials (such as carbon fibre reinforced polymers) as it uses significant power optical excitation sources using a long pulse mode, even though it takes a longer time than pulse thermography [84, 90]. This technique is still growing and offers some advantages over other nondestructive techniques.

The subsurface defects and discontinuities can be successfully found by lock-in thermography, which is more sensitive than pulse thermography. The sensitivity of lock-in thermography is inversely proportional to the depth of the defect. In a specimen, the depth of penetration of low frequency heat waves is higher than high frequency heat waves. As the frequency of heat waves changes, the sensitivity of lock-in thermography also changes. When the depth of penetration for

both high frequency and low frequency thermal waves is the same, lock-in thermography responds more accurately to high frequency thermal waves. High detectivity is achieved in inspection when more than one frequency of waves is used. A defect at a certain depth produces a phase difference which is significantly influenced by inspection frequency. A very small, or no, difference at all may be produced by a defect at a certain frequency. The defect generates maximum positive and negative phase differences at two certain frequencies [94].

Medical Applications of Thermography

The idea of thermography for medical application is well established. The diagnosis and treatment of many ailments is a well known concept where thermal imaging is used to capture and display a heat pattern from the radiation emitted from a patient's body. The setup of thermographic equipment in a clinical setting is generally well controlled within a clean and cool environment. Inflammation, metabolism, and vascularity are three major reasons of surface changes in temperature [95].

Patients with heart diseases have achieved many benefits from the advancement of thermographic technique applications. Thermal angiography [51-53] is used to check the cooling effects of cardioplegia liquids. Patients undergoing bypass [54, 55] surgery also take advantage of intraoperative thermography for the detection of coronary graft flow restrictions [96].

Infrared imaging is better than the standard method of mammography for early detection of breast cancer [56-63]. The temperature of cancer cells are elevated due to their high metabolic activity making it easier to capture by thermography [97].

In order to investigate the results of Chinese medical therapy of acupuncture and Qi-gong (a system of deep breathing exercises), the thermographic method is used to measure the temperature of the hand and arm [98].

Thermal abnormalities during physical exercises or due to diseases, such as malignancies, inflammation, infection, dermatological and rheumatic disorders, can also be detected by skin-contact thermography [86].

Chapter 3 . METHODS AND MATERIALS

3.1 General Approach

The current study developed an FE model of a composite hip implant, which was virtually loaded using axial static forces of 800 N, 1400 N, and 2200 N. An actual composite hip implant was mounted in a mechanical tester and subjected to sinusoidal cyclic loads (average forces, 800 N, 1400 N, and 2200 N) and the surface strains were measured using strain gauges that were mounted on the hip implant. The composite hip implant was then retested without strain gauges using the same cyclic loading regimes as above and its temperature distribution was recorded using an infrared lock-in thermographic camera. All strain gauge values and thermographic temperature values were converted to stress values and compared among the three techniques, namely, FE analysis, strain gauges, and lock-in thermography.

3.2 FE Modeling and Analysis

3.2.1 Geometry

A composite hip implant made of CF/PA12 and its components are shown in Figure 3-1. The hip implant was hollow with an oval cross-section moulded in a shape similar to a human femoral bone, a shaft angle of 135°, a wall thickness of 3 mm, an overall length of 230 mm, a maximum diameter at the proximal base of the neck of 30.3 mm, and a minimum diameter at the distal tip of 15.8 mm as shown in Figure 3-1 (a). The femoral head was made of cobalt-chrome (Figure 3-1b), and the acetabular cup indenter (Figure 3-1 c) was made of stainless steel which was used to apply cyclic loading on the femoral head. The block, as shown in Figure 3-2, was made of cement in which the implant was fixed.

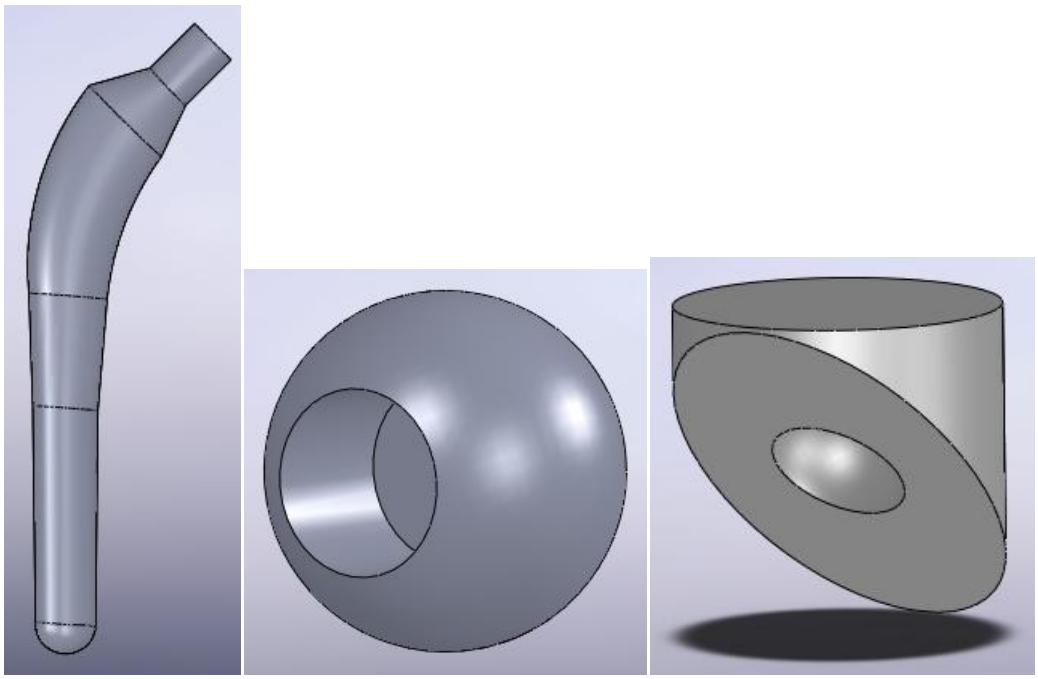

(a) (b) (c)

Figure 3-1 Composite (CF/PA12) Hip Stem and its components. (a). Hip Stem, (b). Femoral Head, (c). Acetabular Cup Indenter

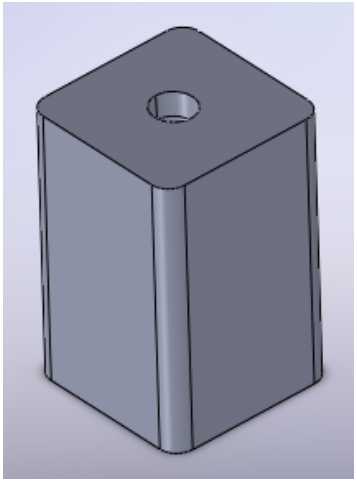

Figure 3-2 Solid works diagram of Cement Block

The front and cross-sectional view of the actual composite hip implant at various locations are shown in Figure 3-3.

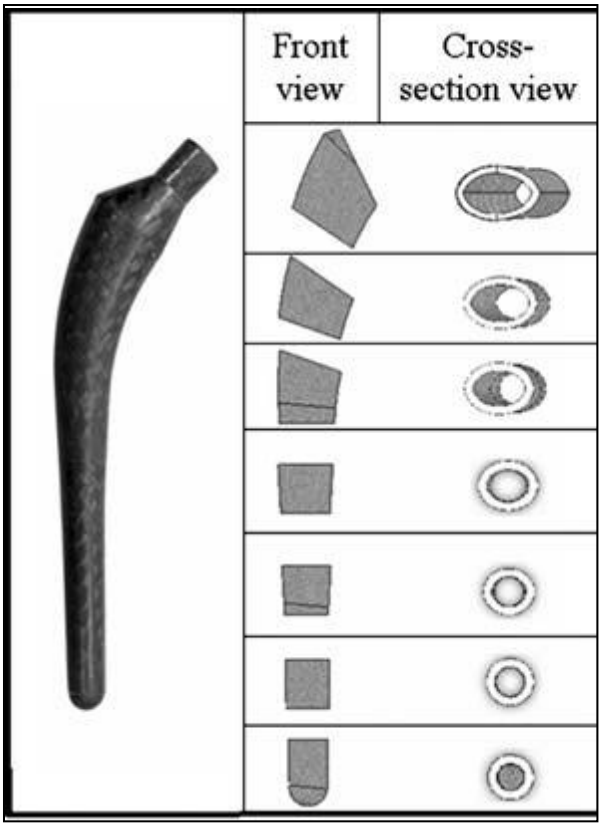

Figure 3-3 CF/PA12 composite femoral stem [41]

3.2.2 Composite Hip Stem Material

In this study, the composite (CF/PA12) material comprising the hip implant material is strong, durable, resilient, biologically inert and has mechanical properties that match the properties of bone. This helps overcome some of the problems being faced by surgeons in implant surgery [99]. Artificial ligaments and fracture fixation devices made of carbon fibre have been used in humans with some success due to its theoretical advantages of flexibility over metallic implants.

Carbon fibre composites have been used in arthroplasty due to their natural tendency to minimize stress shielding, since the material properties match that of human bone. The present composite hip is previously developed to have properties (Table 3-1) identical to that of the contiguous bone into which it can potentially be inserted; this helps in the reduction of bone loss due to stress shielding in the neighbouring femur [45, 100].

Properties	Values
Carbon Fibre Volume Fraction	0.55
Carbon Fibre Weight Fraction	0.68
Density of C F/PA12 (g/cm^3)	1.43
Density of Carbon Fibre (g/cm^3)	1.78
Density of PA12 (g/cm^3)	1.03
Diameter of Carbon Fibres (μm)	10
Diameter of PA12 Fibres(μm)	26
Tensile Strength (MPa)	85
Elongation (%)	13
Flexural Strength (MPa)	130
Flexural Modulus (GPa)	16.4 ± 1.5
Ultimate Strength in Compression (MPa)	155 ± 27
Maximum Load in Compression (kN)	28.6 ± 3.8
Modulus of Elasticity (GPa)	14.5
Specific Heat Capacity (J/kg.K)	485
Thermal Expansion Coefficient (1/°C)	7.64×10^{-6}
Elasticity Model	Linear elastic

Table 3-1 CF/PA12 composite material properties [42]

It has been observed that the composite materials used in orthopaedic applications have good biocompatibility with human tissue and outstanding mechanical properties when surrounded by body fluids. The exceptional handling qualities of fibre and the matrix system, the mouldability

of the composite, the environmental friendly aspects, and the accessibility of light curable matrix systems have contributed to the usage of fibrous components [101]. From prior experimental studies it is observed that the mechanical properties of the currently-used CF/PA12 material for the hip implant are identical to the properties of cortical bone in the femur [41].

3.2.3 Cement Block

In this investigation, the composite hip implant specimen was prepared by fixing its distal tip into a block of cement, i.e. concrete. The concrete block was modelled flexible with properties provided by the material library in the ANSYS Workbench software. Concrete properties are given in Table 3-2.

Properties	**Values**
Density (g/cm^3)	2.3
Elastic Modulus (GPa)	30
Yield Strength (MPa)	0
Ultimate Compressive Strength (MPa)	41
Poisson's Ratio	0.18
Elasticity Model	Linear elastic
Isotropy	Isotropic

Table 3-2 Properties of concrete

3.2.4 Assembly of the components

The distal tip of hip implant was fixed in the cement block. The stainless steel acetabular cup indenter was attached to replicate axial cyclic loading on cobalt-chrome femoral head. Solid Works 2009 was used to draw the CAD model of this assembly in order to simulate the experiment precisely. The geometry was then saved in parasolid file format and was exported to ANSYS Design Modeller where the body operations were executed to assure that no components

overlapped within the assembly. This assembly was exported to the simulation window of ANSYS Workbench 11.0 (ANSYS, Inc., Canonsburg, PA, USA) for analysis. The assembly of composite hip implant in solid works is shown in Figure 3-4.

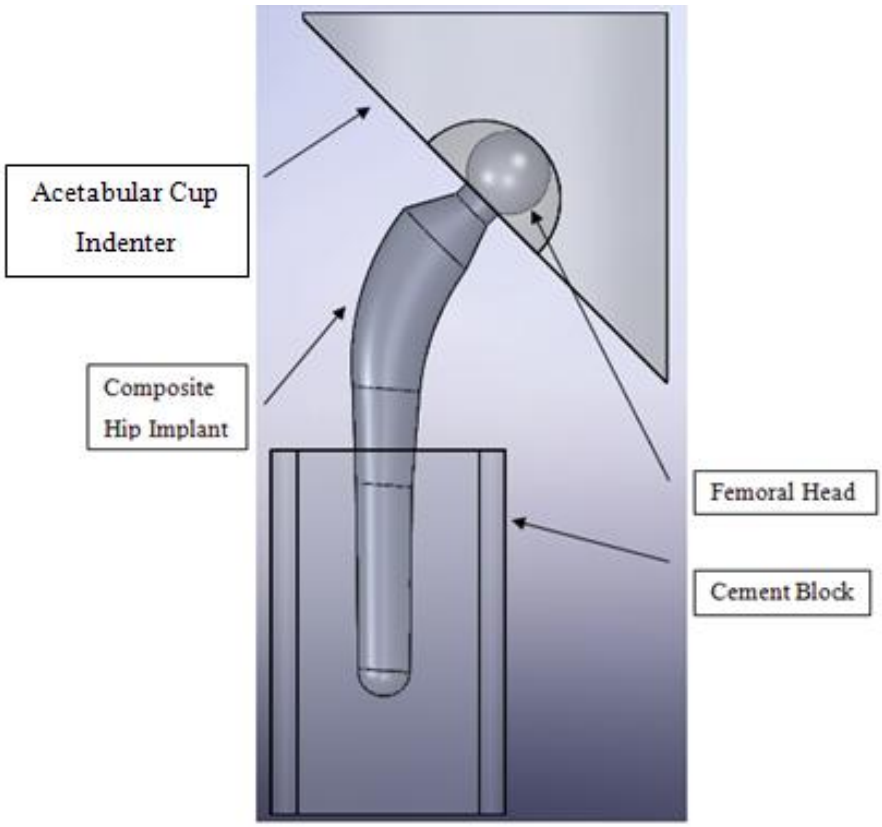

Figure 3-4 Assembly of Composite Hip Implant

3.2.5 Boundary Conditions

The cement block embedded with the composite hip implant was placed in a fixed support, and the acetabular cup indenter was restricted to move in the uniaxial direction only as shown in Figure 3-5. Three different axial forces were applied at a hip implant adduction angle of 15º on the acetabular cup indenter to reproduce the same loading conditions as experienced by the hip joint during regular gait.

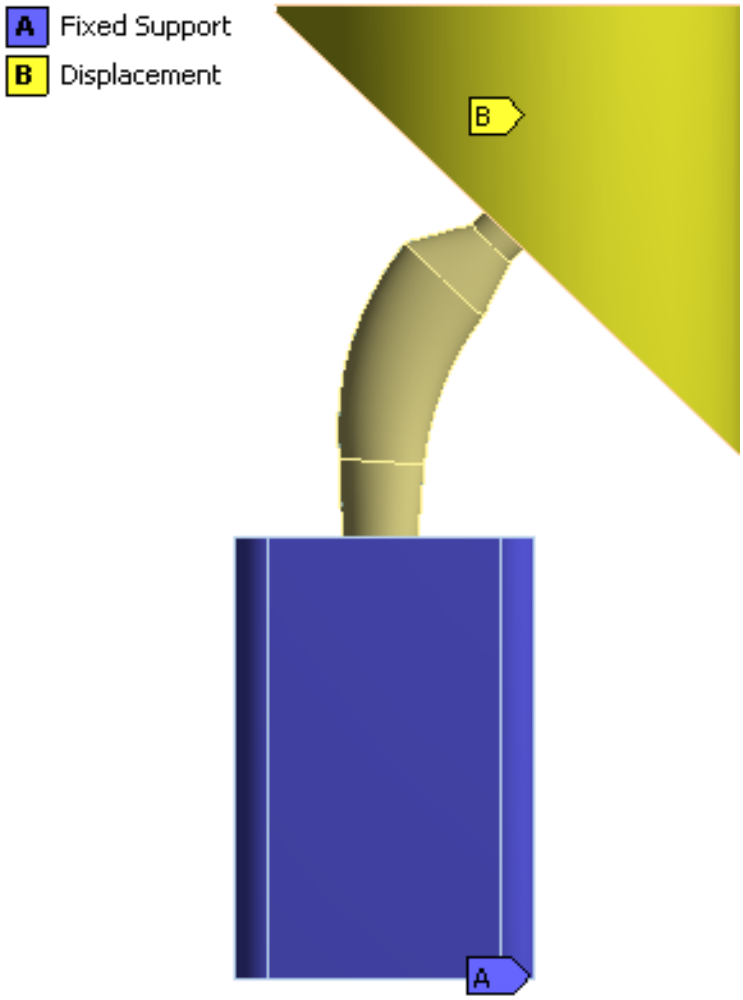

Figure 3-5 Boundary Conditions on the Composite Hip Implant Assembly

All contact surfaces were considered to be bonded, except the region between the acetabular indenter and femoral head was set to 'no separation' in order to avoid slipping at that interface. A model of the hip implant assembly was created in ANSYS software for FEA as shown in Figure 3-6.

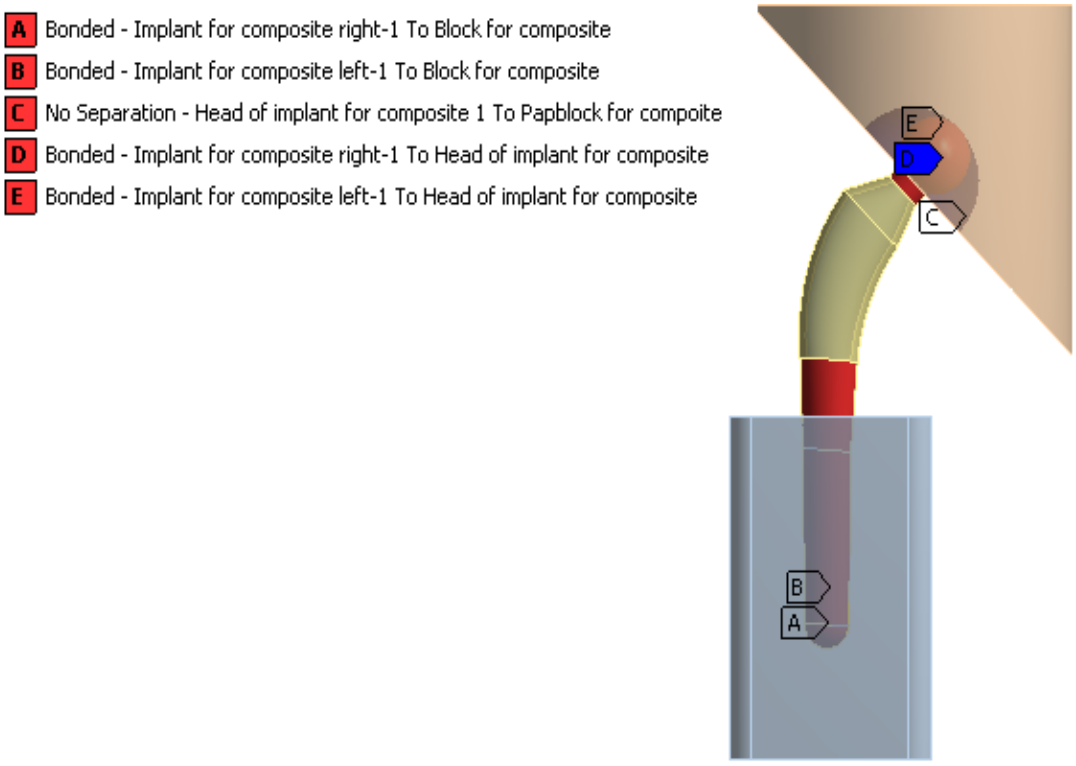

Figure 3-6 Contact locations in the composite hip implant assembly

3.2.6 Meshing Properties and Convergence

Meshes were generated by ANSYS Workbench 11.0 automatically according to input parameters. The number of nodes and elements for the composite hip implant were 88,003 and 58,158 respectively. In order to balance any difficult geometry, the mesh was adjusted accordingly. For the implant, 10-node quadratic tetrahedron structural elements were used. Every element had three degrees of freedom in nodal x, y, and z directions, and the displacement behaviour was quadratic in nature which was able to model irregular geometries imported from CAD software appropriately.

The structural elements for composite hip implants used 10-node quadratic tetrahedron mesh. Four vertices were selected as shown in Figure 3-11. Vertices 1 and 2 were selected on the lateral side, and vertices 3 and 4 were selected on the medial side of the hip stem. Seven meshes were created at 0, 20, 40, 60, 70, 80, and 90% of relevance as shown in Figure 3-7. The 'relevance' utility in ANSYS Workbench was used to carry out refinement until such time that the solution converged adequately. This is a global mesh control utility that permits control of the mesh

fineness and ranges from high speed mesh (-100 setting) to high accuracy (+100 setting). The mesh with a relevance of 90% showed the convergence was achieved in the results.

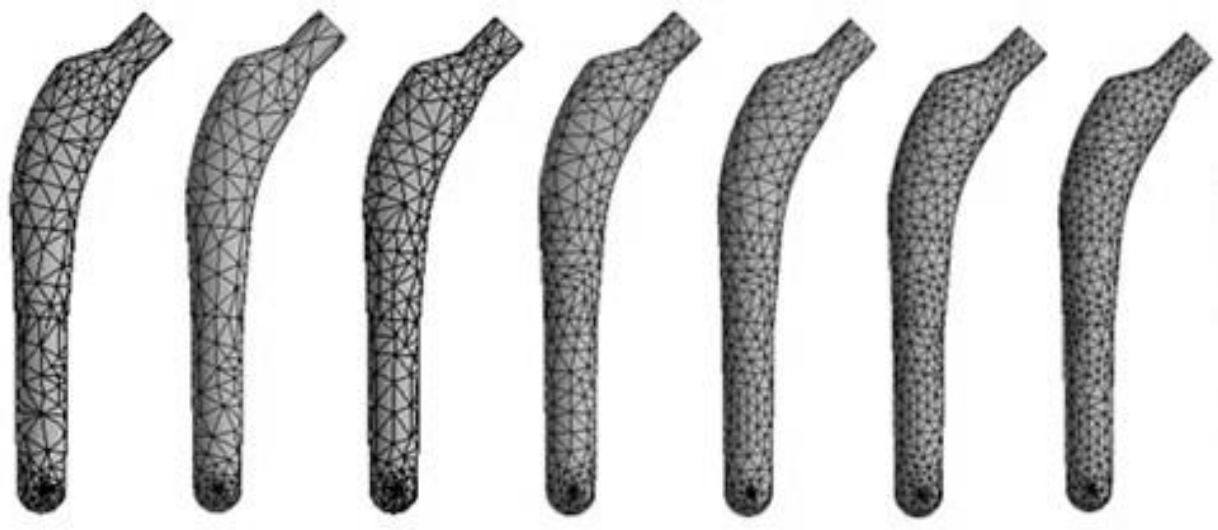

Figure 3-7 Mesh relevance for the composite hip stem (from left to right): 0%, 20%, 40%, 60%, 70%, 80%, and 90%.

The axial loads of 800 N, 1400 N and 2200 N were applied at the hip implant adduction angle of 15° as would be replicated in the experiments which were meant to mimic one-legged weight bearing during the stance phase of walking gait. Von Mises equivalent strains were then recorded after each mesh refinement.

The values of von Mises strains are tabulated in Table 3-3 for different relevance meshes and difference in percentage from the preceding mesh is given within brackets.

Load	Mesh Relevance	Nodes	Elements	Locations of Von Mises Strain Readings with FE strain values (με) (% difference between consecutive relevance values)			
				Vertex 1	Vertex 2	Vertex 3	Vertex 4
800N	90	88003	58158	133 (1.68)	199.4(1.17)	682.9(2.28)	785.9(1.87)
	80	78521	52368	130.8 (4.66)	197.1(1.08)	698.8(1.04)	771.5(2.02)
	70	70266	47105	137.2 (1.40)	195 (2.60)	691.6 (1.83)	787.4(1.73)
	60	63376	42719	135.3 (5.21)	200.2(5.81)	704.5(7.20)	774(1.02)
	40	51286	35265	128.6 (2.13)	189.2(4.35)	657.2(3.60)	782(0.18)
	20	42488	29825	131.4 (1.39)	197.8 (0.40)	681.7 (2.54)	783.4(3.93)
	0	37238	26543	129.6	198.6	699.5	753.8
1400N	90	88003	58158	226.2(3.86)	345.9(1.93)	1216.2(2.23)	1372.5(0.01)
	80	78521	52368	217.8(1.76)	352.7(8.06)	1244(1.46)	1372.7(0.72)
	70	70266	47105	221.7(0.27)	326.4(2.71)	1226.1(86.4)	1382.7(0.47)
	60	63376	42719	222.29(7.18)	335.5(0.42)	1227(89.67)	1389.2(0.71)
	40	51286	35265	207.4(6.66)	334.1(1.88)	1228.9(0.22)	1399.2(2.33)
	20	42488	29825	222.2(7.60)	340.5(1.07)	1231.6(1.05)	1367.3(1.56)
	0	37238	26543	206.5	344.2	1218.8	1346.3
2200N	90	88003	58158	361.3(2.47)	540.4(1.17)	1840.9(2.88)	2172.7(0.88)
	80	78521	52368	352.6(2.17)	546.8(0.11)	1895.5(0.005)	2153.8(0.29)
	70	70266	47105	345.1(5.44)	547.4 (7.14)	1895.6(2.37)	2160.1 (0.42)
	60	63376	42719	327.3(8.24)	510.9 (6.14)	1941.6(0.50)	2169.3(0.62)
	40	51286	35265	356.7(6.16)	544.3 (0.58)	1931.9(0.15)	2156 (0.50)
	20	42488	29825	336(5.93)	547.5(0.33)	1929.1(0.09)	2145.2(0.22)
	0	37238	26543	317.2	549.29	1930.7	2140.4

Table 3-3 Mesh Characteristics, Elements, Nodes and Associated Vertex Microstrains

3.3 Strain Gauge Experimental Setup

3.3.1 Strain Gauge Selection

The first step towards the installation of strain gauges is the selection of a suitable gauge for the required job. The main element which determines the operating features of a strain gauge is the strain-sensitive alloy used in the foil grid [102].

Name	**Description**
Model	CEA-06-125UW-350
Description	Universal General Purpose Strain Gauges
Resistance	350.0 Ω ± 0.3%
Strain Range	±3%
GF Sensitivity	(1.2 ± 0.2) % /100ºC
Gauge Factor, GF (at 24°C)	2.120 ± 0.5%
Temperature Range	-75ºC to 175ºC
Transverse Sensitivity	(0.7 ± 0.2) %
Overall Length and Width	0.325×0.180 in (8.26×4.57 mm)

Table 3-4 Vishay® general purpose strain gauge specifications [102, 103]

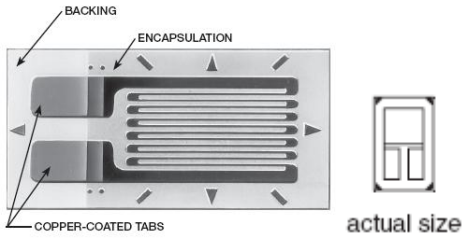

Figure 3-8 Vishay® general purpose linear pattern strain gauge [102]

Sensitivity and precision are the two main reasons considered for the selection of a suitable strain gauge. In general, the measurements respond quicker with high accuracy if more strain gauges are used as in a full bridge circuit instead of a quarter bridge. The price also plays an important role in determining the type of strain gauge that is used. The price of full bridge strain gauges are considerably higher than half and quarter bridge gauges [104].

Selecting a suitable strain gauge depends upon the problem under investigation and the type of specimen on which the gauge will be installed. Other factors playing an important role in gauge selection are temperature sensitivity, high strain sensitivity, and electrical resistivity of the foil [105]. In the current study, the *in vitro* experiments were at room temperature and the specimen had a high elasticity modulus, such that large strain was not possible when the specimen was subjected to compressive loads (up to 2200N).

3.3.2 Strain Gauge Mounting

High resistance gauges (ideally 350 Ω) work better for materials having lower thermal conductivity, such as simulated bone [105]. The loading was done axially as shown in Figure 3-11, and the direction of the strain was also along the same axis, hence uniaxial gauges were considered appropriate. As such, Vishay® 350-Ohms general-purpose uniaxial linear pattern gauges (125UW, model CEA-06-125UW-350, Vishay Micro-Measurements & SR-4, Raleigh, NC, USA) were employed in this study as shown in Figure 3-8.

The first step in installation of strain gauges was degreasing, which was done by wiping the specimen with a sterilized cotton gauze dipped in CSM 2 Degreaser (Vishay Micro-Measurements, Raleigh, NC, USA) [106].

After degreasing, the surface was abraded by using 400-grit silicon-carbide paper to remove any loosely bonded debris such as rust or paint from the surface of the specimen and making it rough for perfect bonding.

A pencil was then used to mark the layout lines on the composite hip implant where the strain gauges were to be installed. This step was followed by applying an ample quantity of M-Prep Conditioner A (Vishay Micro-Measurements, Raleigh, NC, USA) and scrubbing the surface continuously by cotton tipped swab. It was then dried by cotton gauze. The solution was not

permitted to dry on the specimen surface. This was done to remove any contamination from the previous installation step.

The conditioner used was acidic in nature, so in order to neutralize the surface M-Prep Neutralizer 5A (Vishay Micro-Measurements, Raleigh, NC, USA) was applied for rinsing. This was again scrubbed with a cotton tipped swab. Finally, it was dried again [106]

A pair of tweezers was used to remove the gauges from their envelopes and to place them on a piece of PCT-2A cellophane tape (Vishay Micro-Measurements, Raleigh, NC, USA). The taped gauges were positioned on the specimen such that the alignment marks on the gauge matched with the layout lines. For each gauge, one end of the tape was adhered to the surface of the specimen while the other was lifted to expose the bonding side of the gauge. M-Bond 200 (Vishay Micro-Measurements, Raleigh, NC, USA) was applied to the bonding side of the gauge, followed by the addition of a few drops of M-Bond 200 (Vishay Micro-Measurements, Raleigh, NC, USA). The other end of the tape was then placed down on the specimen so that the gauge was perfectly positioned over the layout lines, and firm thumb pressure was applied to ensure that the M-Bond 200 adhesive adhered well. The tape was not removed from the specimen until the wires were soldered to the gauge.

3.3.3 Strain Gauge Measurement

Two strain gauges were connected to one DSub-15-pin connector (ACC/DSUB-UNI2, IMC Mess-Systeme GmbH, Berlin, Germany), as shown in Figure 3-9, in a manner that completed a Wheatstone bridge for strain measurement.

The wiring from the gauges was inserted into numerous labelled slots in the DSub-15-pin connector shown in Figure 3-9. The colour-coded lead wires were separated into three different wires, and 10-15 mm of the insulation was stripped from each coloured wire. The red wire was connected to the +VB1 slot, and the black wire was connected to the I1_1/4B1 slot. A small piece of wire of about 50 mm was taken, and both the ends were stripped. One end of this small wire was inserted into the SENSE1 slot, and the other end of the wire was twisted with the white wire and inserted into the +IN1 slot. This completed the quarter bridge wiring necessary for one strain gauge.

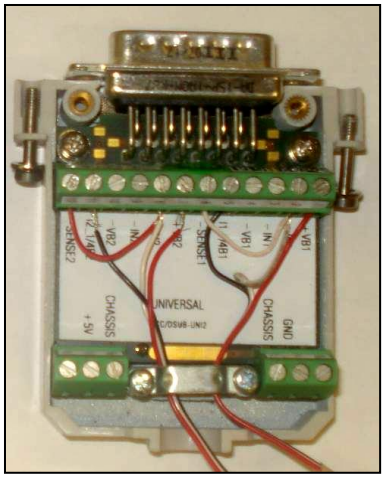

Figure 3-9 A Two-channel Dsub-15-pin connector wired from 2 strain gauges

The same procedure was repeated for all four strain gauges, which were then connected to two separate DSub-15 connectors.

The CRONOS-PL as shown in Figure 3-10 was equipped with a UNI2-8 eight-channel amplifier (IMC Mess-Systeme GmbH, Berlin, Germany), which was connected to one of its posterior slots that served as the interface to hook up two DSub-15 connectors.

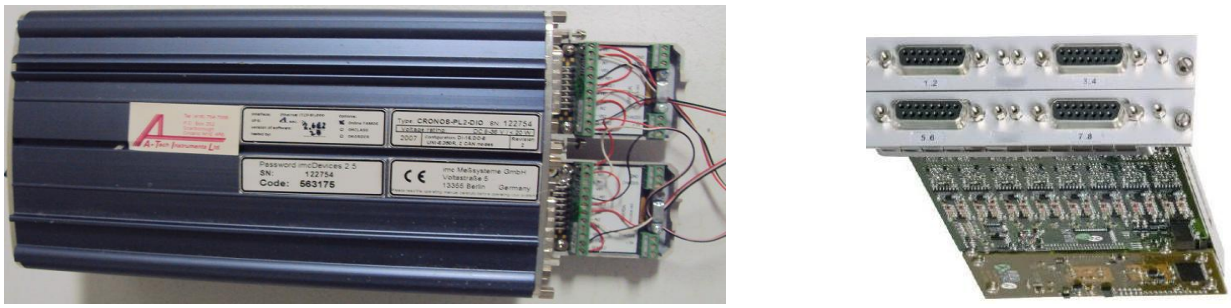

Figure 3-10 DSub-15s Connected to the CRONOS-PL unit (Left) and UNI2-8 eight-channel amplifier (Right)

A laptop computer used to collect data installed with signal analysis FAMOS V5.0 (IMC Mess-Systeme GmbH, Berlin, Germany) was connected to the CRONOS-PL unit by a LAN network. When the strain gauge was configured to the quarter bridge option, a supply of 5 volts was selected in FAMOS V5.0. The gauge factor, resistance and sampling frequency was set at 2.12, 350 Ω and 1.0 millisecond as per the manufacturer's specifications. All strain gauge circuits

were balanced by an option in FAMOS V5.0. The graph of measured strain (in microstrain) was plotted against time for all strain gauges.

The composite hip implant was installed with four 350 Ω general purpose linear pattern strain gauges whose locations are illustrated in Figure 3-11 along with the virtual axial force on its femoral ball.

Figure 3-11 Strain gauge locations with virtual force on femoral head

3.4 Cyclic Loading

An Instron 8874 mechanical tester was used to generate the force patterns on the hip implant for all experiments (Figure 3-13). The load cell had an axial capacity of ±25 kN, a resolution of 0.1 N and an accuracy of ±0.5%. The mechanical tester had a stiffness of 260 kN/mm, which was far greater than was expected for the composite hip implant. Thus, no correction factor was necessary to accommodate for mechanical tester compliance.

The composite hip implant equipped with a metallic femoral ball was cemented into a square-channel steel chamber using commercially-available anchoring cement. This was accomplished by mounting the hip stem onto a chemistry stand using an adjustable multi-axial clamp. The lateral surface was aligned vertically using levelling gauges. The distal tip was lowered and

inserted into the centre of the hollow square-channel steel chambers (88 mm wide X 88 mm wide X 160 mm high). Anchoring cement (Flow-Stone, King Packaged Materials Company, Burlington, ON, Canada) was mixed according to the manufacturer's instructions and poured into the square potting chamber until it was filled to the brim. The cement was allowed to dry 24 hours prior to the specimen being removed from the clamping system. The resulting working length of the hip stem from the top of the potting chambers to the top of the femoral ball was 115 mm. The steel chamber was then distally secured to the base of the tester with an industrial vice at hip implant adduction angle of 15° (Figure 3-11). This angle simulated one-legged weight bearing during the stance phase of gait.

A stainless steel indenter in shape of an acetabulum-like cup was fixed to the machine. A preload of 100 N was applied to prevent any slippage between the femoral ball and the loading cell. Vertical cyclic loads of 800N, 1400N and 2200N (average) were applied to the hip implant at a frequency of 5Hz as shown in Figure 3-12. The waveform was sinusoidal in shape in order to mimic human walking gait loading patterns on the hip joint.

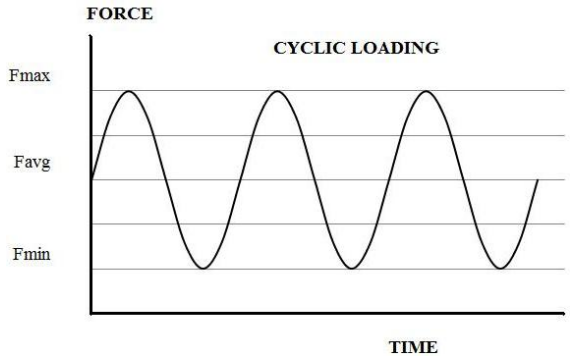

Figure 3-12 Sinusoidal cyclic load application on the hip implant

FastTrack 8800 interface software was used to set the loading rate to 100 N/s. It also recorded displacement from the actuator at every 0.01 seconds in addition to controlling the loading rate and maximum load. The data of actual applied load versus time on the hip implant could then be plotted. The cyclic loading was carried out for 30 seconds, and the FAMOS V5.0 software permitted the plotting of graphs of the strain measurements simultaneously, that were saved for the analysis. Then the actuator was elevated and the pressure was released from the test

assembly. Three test runs were carried out for each loading condition, and a mean reading was calculated for each load.

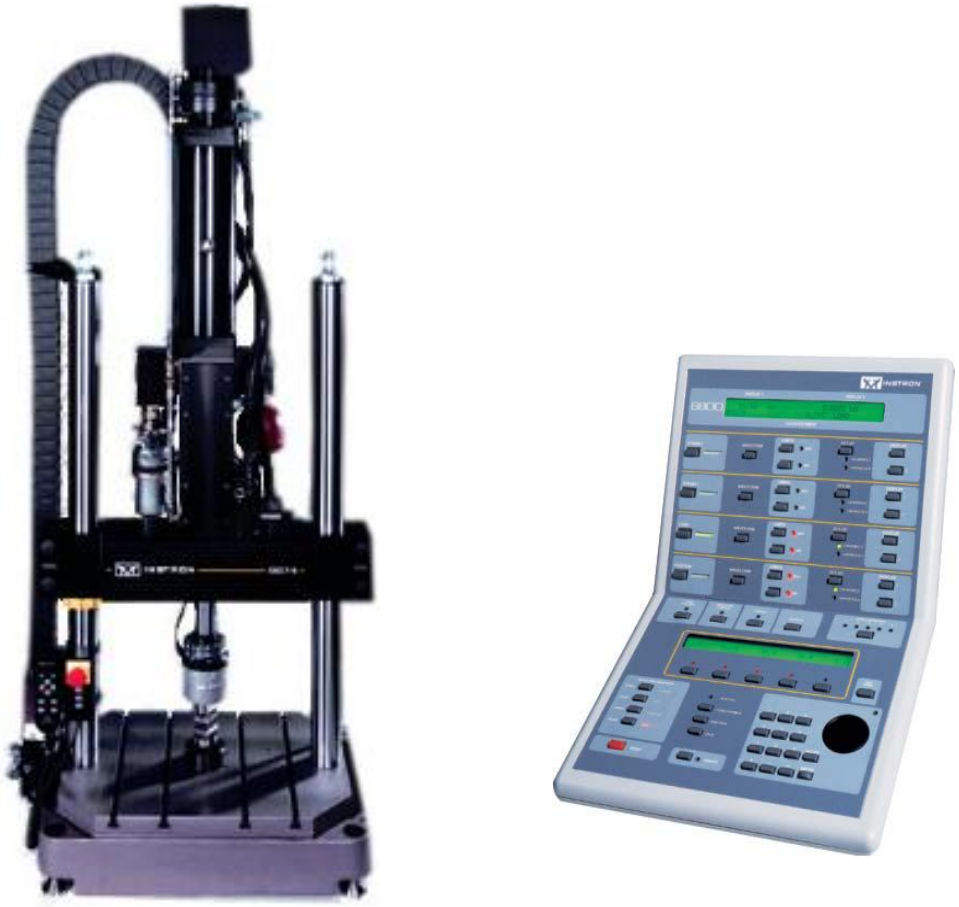

Figure 3-13 Instron® FastTrack™ 8874 (Left)[107]**, Instron® FastTrack™ 8800 Controller Panel (Right)** [108]

3.5 Lock-in Thermography Experimental Test Setup

The current test setup of IR thermography is shown in Figure 3-14. The setup included an IR camera with a spectral window ranging from 3.6 µm to 5.1 µm, a function generator supplying the reference signal, an Instron® FastTrack™ 8874 mechanical tester that applies mechanical loads of varying magnitude on the specimen, a power supply, a lock-in device that synchronizes the infrared frames with the reference signal, and a computer. The measurements were taken with a Silver 420 infrared camera. The ALTAIR-LI software (Cedip Company) installed in a laptop computer was used to monitor the camera. The lock-in box (synchronizing device) helped

in calculating the demodulation of every pixel of the infrared frame. It also stored and displayed the images of the phase shift and front face temperature.

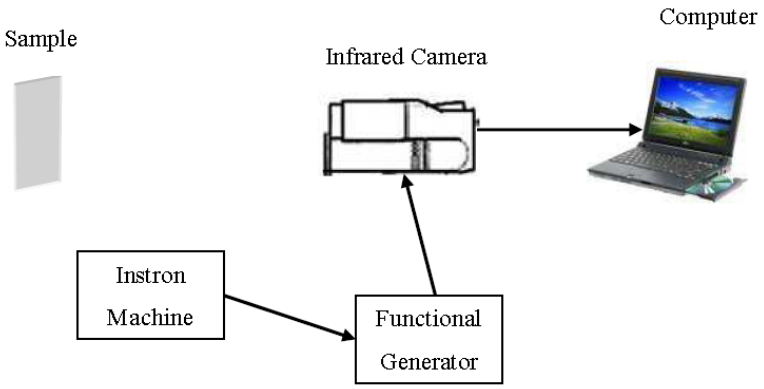

Figure 3-14 Schematic setup of lock-in thermography

The specimen hip implant fixed in a concrete block was gripped in a vice at an angle of 15° at the bottom of the Instron® mechanical tester. Loads of 2200N, 1400N and 800N were applied by the machine. The setup and load application was done in the same manner as described earlier (section 3.4). The only difference was that there was no strain gauge attached to the implant. The thermal camera was mounted on a tripod stand and placed at a distance of about 3 feet (0.91 m) from the specimen. The heat produced in the implant by mechanical excitation was recorded by the thermal camera.

Figure 3-15 Laboratory setup of lock-in thermography

During the inspection, the IR camera was used to record the oscillating surface temperature of the object by taking a series of IR images, on which every pixel represented the average temperature of the matching spot. The camera generated stress maps while averaging the applied force on the sinusoidal waveform. The image recording was synchronised with the modulation frequency, and the IR thermography camera took four images within one cycle as shown in Figure 3-17 .

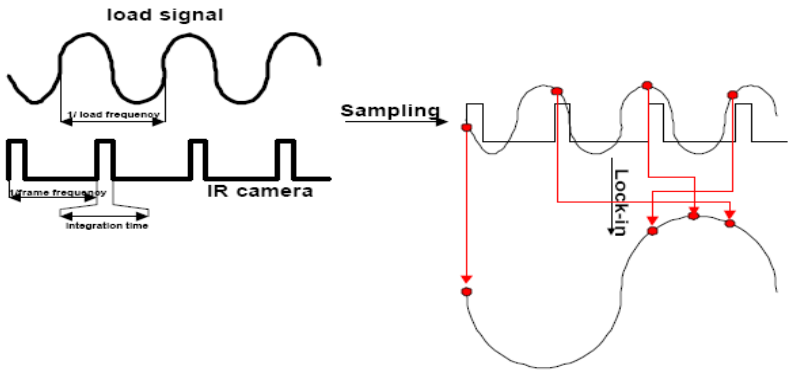

Figure 3-16 Signal analysis of lock-in thermography[109].

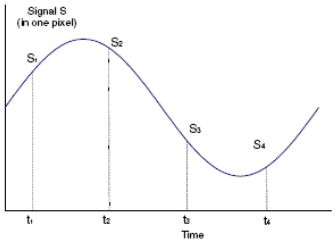

Figure 3-17 Signal acquisition during a thermal wave cycle[90]

The lock-in system obtained four signal values S_1, S_2, S_3 and S_4 in every pixel of the image. The indices refer to the recording time. From these values, the system calculated a phase value (Φ) according to the following basic equation:

$$\Phi = \arctan\left(\frac{S_1 - S_3}{S_2 - S_4}\right) \qquad \textbf{Equation 3.1}$$

Using the Φ values obtained with the above equation, the system produced a phase image. Thermo-elastic stress analysis used in the IR analysis was based on the principle that when a body is compressed, its temperature increases. When the pressure is released, it returns to its

original shape and temperature. The thermo-elastic equation used by the camera to generate stress fields is given below:

$$\Delta T = T \frac{\alpha}{\rho C_p} \Delta \sigma \qquad \textbf{Equation 3.2}$$

where ΔT is change in the temperature, T is the ambient temperature, α is the coefficient of thermal expansion, ρ is the density, Cp is the specific heat capacity and $\Delta\sigma$ is the stress. This equation assumed adiabatic conditions i.e. no significant heat loss. The Altair software used Equation 3.2 to calculate stresses on the surface of the specimen.

The thermal camera used in this study is a Silver 420 Infrared Camera. Its sensitivity, precision and speed are optimal for conducting thermal and radiometric measurements. The camera had 320 X 256 pixels, each of which corresponded to a pixel of the image. The size of each pixel was 30μm X 30μm and was at a distance of 5μm from the adjacent pixel. This resolution gave high sensitivity and at the same time offered an adequate dynamic range with perfect linearity. The frequency of the image could be programmed, and subwindowing modes were uncomplicated and flexible.

This camera had a power driven built-in auto focus 27 mm lens and the focusing of the object was done by control buttons in the program software. In order to examine a specimen, it was necessary to make sure that it was located in the middle of the image and focusing was done appropriately. A BNC 75 ohms cable was used to connect the camera to a video monitor in order to control the image [110]. A picture of the camera used is given in Figure 3-18.

Figure 3-18 Silver 420 thermal camera[110]

Technical data are given below for the camera used in this study (Table 3-5).

Parameters	Values
Spectral Response (Wavelength)	3.6 µm – 5.1 µm
Subwindow	160 x 120 pixels / 80 x 60 pixels / 64 x 8 pixels
Frame Rate	5 Hz to 170 Hz full Frame
Image Capture	Snapshot Integrate then Read mode (ITR)
Number of Pixels	320 x 256 pixels
Pitch	30 µ m x 30 µm
Cooling Type	Integral stirling Cooler
Cooling Time	< 7mn @ 25°C ambient
Frame Rate Resolution	1 Hz step
Resolution	1 MPa
Power Supply	12 VDC / 5A
Power Consumption	50W in cool down mode, 30W in steady state mode
Digital video	USB / Cam LINK
Analogue Video	PAL (50 Hz) or NTSC (60 Hz)
Remote Control	USB / Cam LINK
Overall dimension (mm)	310 x 141 x 159
Weight	3.8 kg
Operational Temperature range	-20°C + 55°C

Table 3-5 Technical data for the Silver 420 infrared camera [110]

Chapter 4 . RESULTS

4.1 Finite Element Analysis Results

The static strain values calculated from the finite element analysis model are tabulated in Table 4-1. The locations are identified and correspond to the gauge locations as mounted during strain gauge experiments. It was evident from the results that the lateral side of the implant experienced tension while the medial side was under compression. All the strain values are given in μm/mm.

Vertex	Location	Calculated strain (με) from FEA			State of load experienced
		2200 N	1400 N	800 N	
1	Lateral	361	226	133	Tension
2	Lateral	540	345	199	Tension
3	Medial	1840	1216	682	Compression
4	Medial	2172	1372	785	Compression

Table 4-1 Microstrain values calculated by Finite Element Analysis

4.2 Strain Gauge Results

The measured cyclic strains from the experiment are tabulated in Table 4-2, and the position of each gauge is identified. The trend for the state of load experienced by the implant was identical to that of the FE model, with tension on the lateral side and compression on the medial side.

Vertex	Location	Measured strain (με) from Experiment			State of load experienced
		2200 N	1400 N	800 N	
1	Lateral	450	275	190	Tension
2	Lateral	475	275	200	Tension
3	Medial	1400	800	580	Compression
4	Medial	520	325	220	Compression

Table 4-2 Microstrain values obtained by strain gauges

4.3 Stress Values obtained from IR Thermography

The values of cyclic stress obtained from lock-in thermography for 800 N, 1400 N and 2200 N are tabulated in Table 4-3. The same tension and compression trends of stress distribution on the lateral and medial sides, respectively, were observed from thermography.

Vertex	Location	Measured stress (MPa) from IR Thermography			State of load experienced
		2200 N	1400N	800 N	
1	Lateral	8.44	4.19	3.5	Tension
2	Lateral	7.46	4.21	1.58	Tension
3	Medial	20.3	12.09	7.1	Compression
4	Medial	11.73	4.97	3.1	Compression

Table 4-3 Stress values obtained from IR thermography

4.4 Comparison of Strain from Strain Gauge Experiments and FEA

The strain values from FEA and strain gauges for the axial loads of 800N, 1400N and 2200N are given in Table 4-4. Vertices 1 and 2 located on the lateral side of the implant experienced tension while the vertices 3 and 4 located on the medial side were under compression. Actual strain readings from FEA are given in Appendix 1 as Figure A1-1, A1-2 and A1-3.

Von Mises Strain (με)												
Load	Vertex1(Tension)			Vertex 2 (Tension)			Vertex 3 (Compression)			Vertex 4 (Compression)		
	FEA	Strain Gauge	%	FEA	Strain Gauge	%	FEA	Strain Gauge	%	FEA	Strain Gauge	%
2200N	361	450	19.78	540	475	-13.68	1840	1400	-31.43	2172	520	-317.69
1400N	226	275	17.82	345	275	-25.45	1216	800	-52.00	1372	325	-322.15
800N	133	190	30.00	199	200	0.50	682	580	-17.59	785	220	-256.82

$$\%Difference = \frac{(Experimental\ Strain - FEA\ Strain)}{Experimental\ Strain} \times 100$$

Table 4-4 Comparison of equivalent Von Mises Strains obtained from FEA and Strain gauges.

The strain values obtained from the finite element analysis were compared to the strain values measured from the strain gauge experiments to verify if FEA could be used to predict the strain distribution in the composite hip implant. Eight of the twelve readings from strain gauge experiment agreed well with FEA predicted results (within 0.5- 31%). The reading for strain gauge (vertex 4) installed near the distal tip of the implant had high disagreement. A correlation graph was plotted by considering only three gauge locations. A slope of greater than 1 showed that FEA overestimated the strain values when compared to the experimental results (Figure 4-1). The correlation coefficient R^2=0.98 showed very good agreement between the two sets of values of the strains from FEA and strain gauges. The slope of the graph is the measure of reliability which indicates the accuracy of the results and R^2 is the measure of repeatability which indicates the precision in the results.There was a nominal experimental 'offset' strain value due to experimental preload, which corresponded to the zero FE strain.

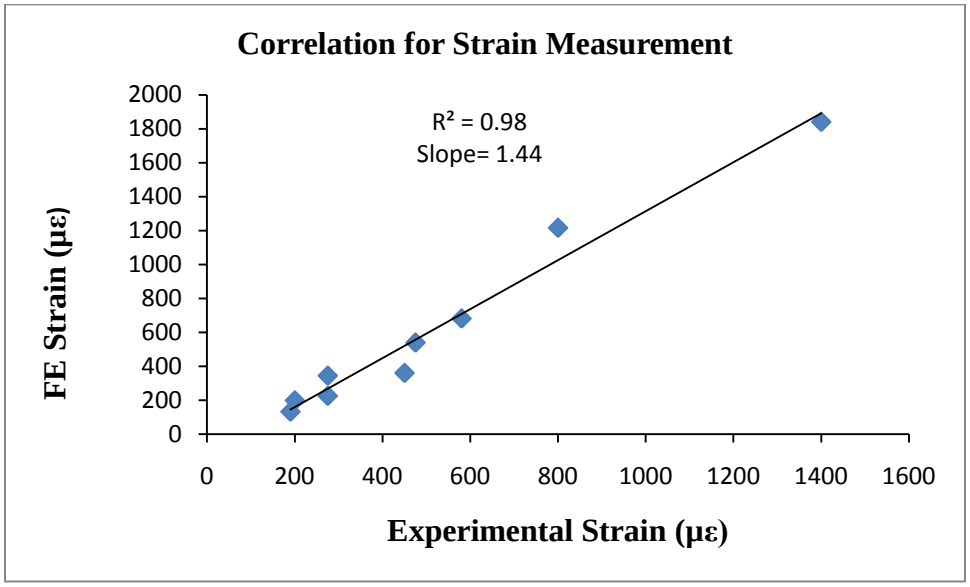

Figure 4-1 Correlation graph for all values of strain (excluding vertex 4) at 2200N, 1400N and 800N from FEA and Strain Gauges.

4.5 Comparison of Stress from Strain Gauge Experiment and IR Thermography

Hooke's law was used to calculate stress values from strain gauge results by using modulus of elasticity of the composite as 14.5 GPa. The stress values calculated from the strain gauge results for axial loads of 800 N, 1400 N and 2200 N are given in Table 4-5, and compared with the

corresponding stress values obtained by lock-in thermography with the help of a thermal camera. The actual stress readings are labeled on two-dimensional thermograms obtained from lock-in thermography for individual load at each location and are given in Appendix 2 as Figure A2-1, A2-2, and A2-3.

Stress				
Vertex	Load Applied	Reading from Strain Gauge (MPa)	IR Stress (MPa)	%
1	2200N	6.53	8.44	-29.25
2		6.89	7.46	-8.27
3		20.30	20.33	-0.15
4		7.54	11.73	-55.57
1	1400 N	3.99	4.19	-5.01
2		3.99	4.21	-5.51
3		11.60	12.09	-4.22
4		4.71	4.97	-5.52
1	800 N	2.76	3.5	-26.81
2		2.90	1.58	45.52
3		8.41	7.1	15.58
4		3.19	3.1	2.82
$\%Difference = \frac{(Strain\,Gauge\,Stress - IR\,Stress)}{Strain\,Gauge} \times 100$				

Table 4-5 Comparison of stresses obtained from Strain Gauges and IR

The values of stress at vertex 3 are higher in both cases. From FEA, strain gauges and thermographic results it was evident that vertex 3 was located in an area of stress concentration.

The correlation graph of the results from thermography and strain gauges showed strong correlation with a slope = 1.01 and a correlation coefficient of R^2 = 0.96 (Figure 4-2). The slope of the graph showed IR thermography overestimated the stress values when compared to strain gauge results. There appeared to be no nominal 'offset' stress value when comparing strain gauge stresses versus IR stress measurements, since during both tests a preload was applied on the hip implant.

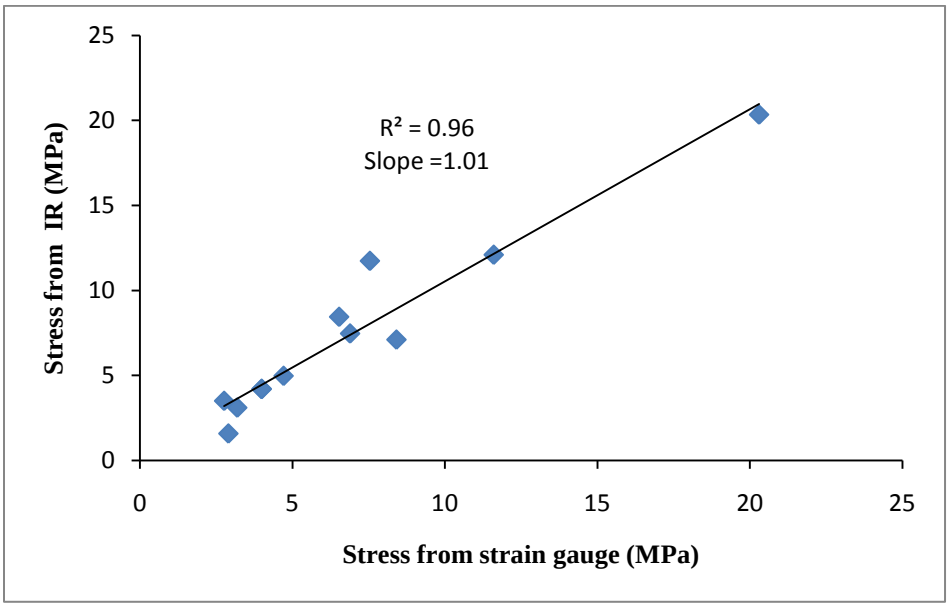

Figure 4-2 Correlation graph for all values of stress at 2200N, 1400N and 800N from strain gauges and IR.

Chapter 5 . DISCUSSION

5.1 General Findings from the Current Study

The present FEA and strain gauge experimental studies suggested that thermography could be used to investigate the stress/strain distribution in a composite hip implant with confidence. The results obtained by these methods were comparable with strong correlation. Thermography, like FEA, gave full stress maps making it easier to locate stress concentration points at a glance which was not possible in strain gauge experiments.

5.2 Comparison of Strain from Strain Gauges and FEA

Three out of four strain gauge readings agreed well with the FEA results and were within 30% for all three loading conditions, while for vertex 4 the readings differed exponentially. The strain value at vertex 3 was very high for both FEA and strain gauge experimental study for all loading conditions. It was most likely due to the geometry of the hip implant, as this location was extremely curved where strain gradients may be expected to change rapidly. The size of the strain gauge foil was comparatively large, which made it difficult to obtain consistent uni-axial readings over a curved surface. At the level of microstrains, a similarity within 30% is a convincing validation of the FE model. The FEA predicted very high values of strain at vertex 4. This location was nearest to the cement block constrained from all sides providing high stiffness which could be the reason for such high values.

A slope of greater than 1 showed that FEA overestimated the strain values when compared to the experimental results (Figure 4-1). The correlation coefficient R^2=0.98 showed very good agreement between the two sets of values of the strains from FEA and strain gauges. The slope of the graph is the measure of reliability which indicates the accuracy of the results, and R^2 is the measure of repeatability which indicates the precision in the results.

Strain gauges are ideally meant to measure the value of strain on a flat surface. It gives the average value of strain under the foil while the FEA gives a nodal value of strain at a particular point. Slight misalignment of the gauge with the vertical axis of the specimen may also have

influenced the present results. The correlation graphs showed strong agreement between the values of strain obtained from the FE model and the experimental strain gauges.

The force displacement graphs for the applied loads of 800N, 1400N and 2200N indicated that the hip implant remained within the linear elastic limit. No permanent damage ocurred to the hip implants during mechanical testing. The value of the linearity coefficient remained at $R^2 = 0.99$ for all three loads utilized.

5.3 Comparison of Stress from Strain Gauges and IR Thermography

The value of stress was high at vertex 3 as compared to the other three values. This was true for all three applied loads. This was due to the curved geometry of the neck of the implant. The strain gradient was expected to change rapidly in this area. Only 4 out of 12 readings showed a high degree of disagreement between the stresses. The correlation graph showed excellent agreement ($R^2 = 0.96$, slope = 1.01) between the values of stress obtained from lock-in thermography and experimental strain gauges.

5.4 Comparison of Present FEA Results to Prior Studies

Bougherara *et al.* [45] conducted FE analysis on three solid models of the implant, namely, an intact femur, a titanium-based alloy hip implant (Young's Modulus, 110 GPa; Poisson's Ratio, 0.3), and a biomimetic composite hip implant (CF/PA12). A load of 3000N was applied on the femoral head at an adduction angle of 20°. Peak maximum stress in the composite implant was observed to be 72 MPa. Bone resorption and implant loosening could be minimized if the composite hip implant was used. In the current study, the maximum stress was 52.74 MPa when a load of 2200N was applied at an angle of 15°. At present, by interpolating the stress value for 3000N, the result achieved was 71.9 MPa, which was almost identical to the value observed by Bougherara *et al.*

Rohlmann *et al.* [111] used FE modelling to determine stress distribution in a hip implant and studied the influence of design and material properties of implants, cement, and surrounding bone. The modulus of elasticity of the implant was 200GPa, and Poisson's ratio was assumed to be 0.33. A force of 2670 N was applied on the femoral head of the implant. Geometric and

material data were taken from the actual bone. They conducted the same test and used 34 strain gauges to validate the results. Reasonable agreement (difference of 12.7%) was found between experimental and analytical results on the outside of the femur. In the current study, the modulus of elasticity for the implant was very low at 14.5 GPa and good agreement (difference of 30%) was observed between FEA and the experimental measurements.

Viceconti *et al*. [112] used two hip implants made up of Ti6A14V (E=110GPa) and installed 7 strain gauges on the lateral side. The stems were cemented in a steel cup and loaded with a force from 30 to 3300N. The tensile stresses were measured as 436 MPa and 405 MPa respectively on both stems. Then 3D CAD models were exported to a finite element program and analyzed. The experiments were simulated and the results for tensile stresses were 466 MPa and 438 MPa respectively. The strain calculated was 0.00423 mm/mm. The agreement between the results of experimental tests and FE analysis were within 7 to 8 %. At present, considering the axial load of 2200N, it was concluded the strain value was 0.00363 mm/mm, which was close to the results of the study conducted by Viceconti *et al.*

Helgason *et al.* [113] used FE analysis to assess the risk of implant failure during walking gait. The implant was made from Ti-6Al-V, and Young's modulus and Poisson's ratio were set as 110GPa and 0.3 respectively. They set the value of failure at 493MPa which was equal to a Von Mises equivalent stress of fatigue failure of ASTM grade 5Ti–6Al–4V alloy. Varying forces were applied in the range of 803 N to 1014 N. It was found that a maximum stress of 47.2 MPa was present around the implant on the outer posterior surface of the bone at the proximal end of the implant, whereas a 61.5 MPa Von Mises stress were found in the proximal part of the diaphysis. The measured strain for the proximal part of the diaphysis was 558 με. In the current study, the value of strain was predicted to be 682 με at the corresponding location for the applied load of 800 N. There was a difference of 18% in the results.

Overall, in most previous studies, FE analysis was used to conduct analysis on metallic hip implant models, which was likely the cause of most discrepancies when comparing prior results to current stress and/or strain data. Bougherara *et al.* [75], however, used a composite hip implant model, thereby yielding results that were similar to the present study.

5.5 Comparison of Present Experimental Strain Gauge Results to Prior Studies

Khursheed [114] conducted similar tests on a CF/PA12 composite hip implant. The implant was subjected to an axial load of 3000 N at an adduction angle of 0°. It was observed that the lateral side of the implant experienced microstrains in the range of 1017-1274 με and the medial side experienced microstrains between 2352 to 4178 με. In the present study, the trend of the strain experienced on lateral and medial was similar to this prior study, i.e., tension on the lateral side and compression on the medial side. The values of microstrains were higher on the medial side ranging from 580 to 1400 με and lower on the lateral side ranging from 450 to 475 με when an angular load of 2200 N was applied on the femoral head.

Akay *et al.* [115] used a CF/PEEK composite implant (E=16.4 GPa) and subjected it to 3000N load at an angle of 20º to the shaft of the femur. Six strain gauges were positioned on the lateral site of the implant and five strain gauges on the medial side. The maximum tensile stress on the lateral side of the stem was 30 MPa, and the maximum compressive stress on the medial side of the stem was 45 MPa. Presently, the compressive stresses on the medial side were also higher than the tensile stresses on the lateral side. The compressive stress of 20.3 MPa on the medial side of the implant is in good agreement for the 2200N load.

Otani *et al.* [116] studied the impact of flexible carbon composite femoral component (E=18.6 GPa), a titanium alloy implant (E=100GPa), and a stainless steel implant (E=200GPa) in a proximal composite femur (fibre glass reinforced epoxy). In their study, strain gauges were installed at 8 locations on the proximal femur and subjected to axial loads of 1000 N and 2000 N at an adduction angle of 9º. Due to this axial loading, it was observed that the compressive strain at the calcar region was considerably higher in the intact femur and the carbon composite hip implant in comparison with two other hip implants. There was not a big difference between the strains measured in the femur and carbon composite hip implant. In the current study, however, the implant was not fixed in the femur and force was applied directly on the femoral ball attached to the implant, making direct comparison of results to the prior study problematic.

O'Connor *et al.* [117] measured *in vitro* strains in the cement mantle around a hip implant by using strain gauges fixed inside the cement mantle. The hip stem was implanted into a cadaveric human femur that was subjected to physiologic loads replicating both single-limb posture (800

N) at an adduction angle of 15º to the vertical and stair-climbing (1780 N) at an abduction angle of 20º. It was observed that the highest values of the strain were at the most proximal section of the cement mantle near the tip of the hip implant. These two areas were known to experience high strain, cement debonding, and cement mantle failure. From the strain gauge data, it was concluded that during stair climbing the cement mantle in the proximal section experienced highest value of the strain while the tip of the implant experienced high strain in both gait and stair-climbing. In the current study, the strain distribution was measured for the hip implant itself and not the surrounding area, making direct comparison of the results to the previous investigation difficult.

Simões *et al*. [118] used 5 Freeman's prosthetic hip implants made of steel (E=210GPa), aluminum (E=70 GPa), composite (E=12 GPa) and polyurethane to conduct tests. The replicas of intact and implanted femur models of the human femur were made from glass fibre-reinforced-epoxy and polyurethane foam. Four strain gauges were installed at lateral, medial, anterior and posterior parts of the femur, and a force of 1000 N was applied. It was observed that the strain distribution at the lateral and medial parts of the implanted femur was the same as in intact femur. The stiffer prostheses promoted higher strain variation in the calcar region of the femur. In the current study, however, only one implant made of composite material was analyzed that was potted directly into a cement block without a femur, and strain was measured on its surface directly. Thus, a direct comparison of surface strains and stresses on the hip implant with Simões *et al.* is problematic.

5.6 Clinical Relevance

The current results showed that the highest strains and stresses occurred in the proximal region of the hip implant, especially in the neck region. This suggests that this zone would be particularly susceptible to failure if this composite hip implant were to ever be inserted into a human femur *in vivo* and subjected to physiological loading conditions over a long period of time. This potential failure site of high stresses has been noted by Bougherara *et al.* in a prior FE and experimental study that used metallic hip implants virtually mounted into an FE model of a synthetic femur representing healthy bone stock [119]. They reported FE peak stresses of 190 MPa and 141 MPa in two different hip prostheses in the superior region of the neck, whereas the

peak stresses on the bone at the distal site of implant insertion into femurs were 11 MPa and 22 MPa, respectively.

As such, the good bone stock of healthy human femurs could provide a rigid fixation which would allow high stresses to develop in the composite hip implant's neck region, predisposing it to potential failure. Conversely, the poor bone stock arising from severe osteopenia or osteoporosis may not permit the composite hip implant to be anchored firmly, thereby causing the site of implant failure, loosening, or migration to be in the distal region where the implant is in direct contact with the bone. To prove these suggestions, future biomechanical tests *in vitro* would need to be done in which the composite hip device is implanted into synthetic or human cadaveric femurs mimicking high and low quality bone stock.

As this composite material matches the properties of a cortical bone, it may prevent loosening of the hip implant, which sometimes occurs due to "stress shielding", being one cause for revision surgery for hip implant patients.

Lock-in thermography can be successfully used for quality assurance of a polymeric composite hip implants. It gives a full stress map on the surface of the specimen for cyclic loading regimes. This technique is easy to use and should, therefore, be explored more comprehensively for clinical application.

5.7 Limitations and Future Considerations

The FE study was based only on static analysis of the hip implant, while the strain gauge and thermographic experiments were carried out with cyclic loading of the implant. El'Sheikh *et al.* [120] reported that dynamic effects provided 10% to 20% more loading on an implant. Moreover, cyclic loading is a more clinically and physiologically realistic scenario that represents the walking gait, which can generate forces of 3 to 4 times body weight at the hip joint [121, 122].

The composite hip implant was considered to be linear and isotropic in order to simplify the FE analysis. However, future studies may wish to consider taking into account any non-linear and visco-elastic properties of the hip implant.

The concrete block with a potted hip implant was gripped in a vice during the experimental and thermographic study, which provided rigid constraints only on two faces of the block. However, the FE model developed had rigid constraints on all sides of the block. Also, the square steel chamber which housed the cement and the distal portion of the hip implant was not incorporated into the FE model; it was assumed this would only add negligible stiffness to the distal boundary conditions. These differences might have been the cause for any discrepancies in the results when comparing FEA with the experimental test modalities.

The experimental tests were limited to the linear elastic limit of the material. Fatigue failure should also be considered in order to understand more comprehensively the behaviour of implants under dynamic conditions that simulated long-term use by a patient.

Only one hip implant sample was tested for the current study which could be increased to a number of samples so that a more thorough statistical comparison could be carried out.

The composite hip implant was tested in isolation, without being mounted in a cadaveric or synthetic femur, which would have been a more clinically realistic scenario.

The complex geometry of the implant near the neck produced stress concentrations during the manufacturing process. Moreover, strain gradients could be expected to change rapidly in this curved area. The size of the strain gauge foil was comparatively large, which made it difficult to get consistent uni-axial readings over a curved surface. These factors might have led to higher values of stress and strain at vertex 3.

Linear strain gauges do not work optimally on curved surfaces because they are ideally meant for flat surfaces in order to yield normal strain values. Moreover, they are physically fragile and may peel or unglue easily, thereby yielding unstable voltage signals and unstable strain results. Both of these factors may have influenced the present results.

The femoral head of the implant was covered with tape so that slippage could be avoided between the acetabular cup indenter and the femoral head when load was applied by the Instron machine. The friction characteristics of this interface, however, were not measured and may have affected the results.

The blurry images from the camera might be due to lack of focusing and environmental thermal noise around the specimen. The acetabular cup indenter geometry prevented thermographic images from being taken on the medial side of the implant. The cup can be optimised and redesigned so that the images can be recorded from any side to provide a more comprehensive investigation of the hip implant.

The load versus displacement graphs from cyclic experiments showed some data scattering and drift, which could have been caused by vibration of the load cell actuator of the Instron machines, slippage of the femoral ball inside the metal acetabular cup, slippage of the cement block inside the industrial clamping mechanism used to fix the specimen distally, and/or a drift in the stiffness of the composite hip implant material with each subsequent cycle of load. Even so, the linear correlation coefficient for these graphs was close to 1, indicating that the specimen was kept within the linear elastic region during tests.

The waveform used in this experiment was sinusoidal to mimic human walking. However, future studies may wish to consider triangle or other cyclic waveform to study its effects on stress distribution on the specimen surface.

Chapter 6 . CONCLUSION

Lock-in thermography can be used effectively for nondestructive evaluation of a polymer composite (CF/PA12) hip implant. The results achieved by this method were comparable to those of strain gauges and FEA. It is a noncontact technique which can cover a large test area with minimal effort.

The mechanical properties and behaviour of the composite hip implant were first analyzed by using strain gauges and FE analysis when it was subjected to different axial loads. The FE model results and strain gauge results were comparable within 9% for three out of four vertices. The fourth vertex, however, demonstrated a higher degree of discrepancy. Pearson's correlation and slope between the two techniques showed good agreement.

The experiment was repeated using the IR thermal camera to record thermal images. Stresses were measured directly with the help of a thermal camera and software. These stresses were compared to stresses already measured from the strain gauges. The correlation graph between the two sets of values yielded R^2=0.96.

Lock-in thermography is a new technique which yields full stress maps, whose results are comparable to the local strain results obtained through conventional techniques employing strain gauge measurements.

APPENDICES

APPENDIX 1: Results from Finite Element Analysis

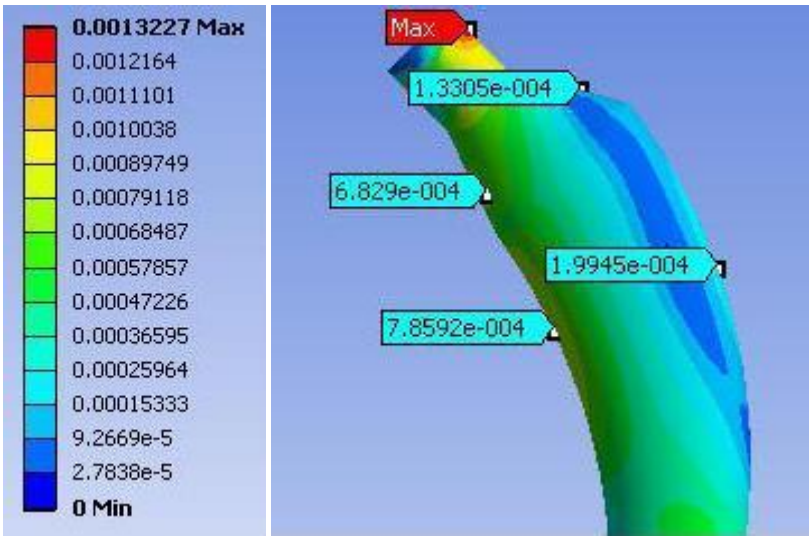

Figure A1- 1 Von Mises strain values (mm/mm) for 800N

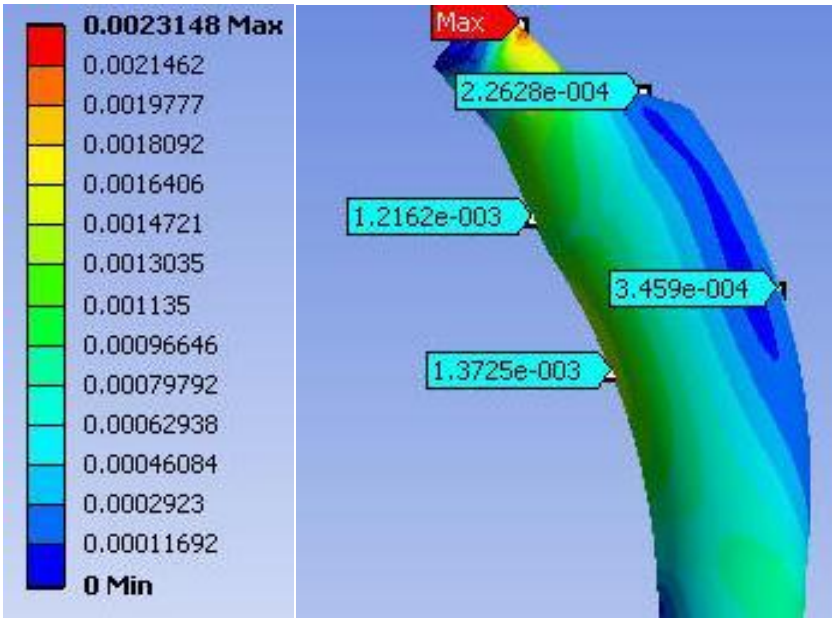

Figure A1- 2 Von Mises strain values (mm/mm) for 1400N

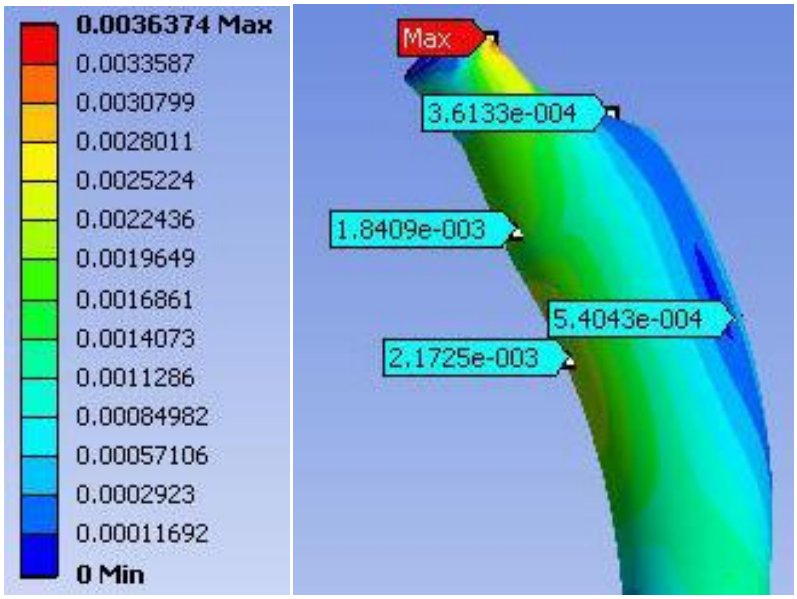

Figure A1- 3 Von Mises strain values (mm/mm) for 2200N

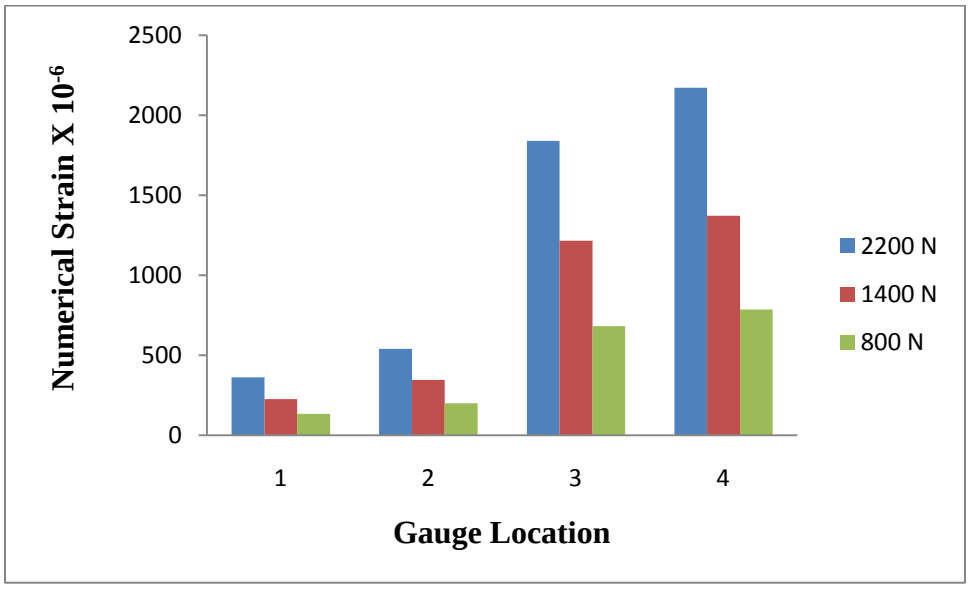

Figure A1- 4 Bar chart for microstrain values obtained by Finite Element Analysis

Load	Maximum stress (MPa) calculated from FEA
800 N	19.17
1400 N	33.56
2200 N	52.74
$Stress = Strain \times Young's\ Modulus$	

Table A1- 1 Stress values calculated from FEA strain

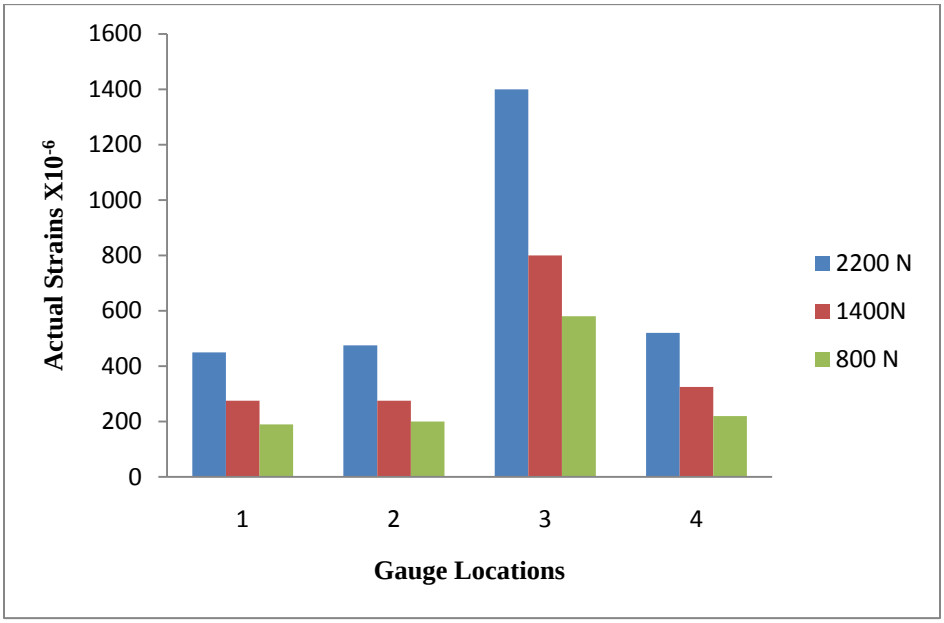

Figure A1- 5 Bar chart for microstrain values obtained by strain gauges

APPENDIX 2: Results from Infrared Thermography

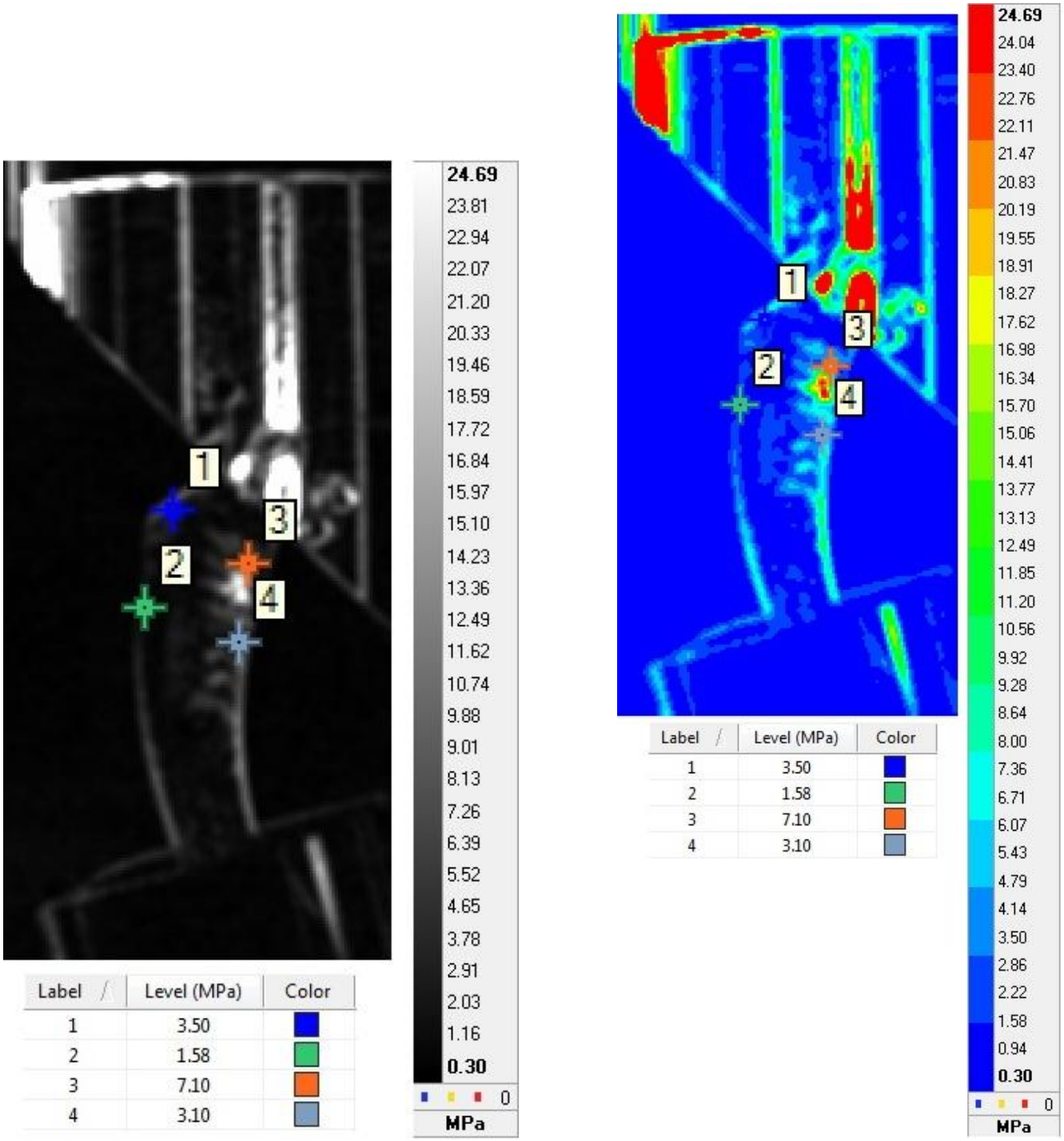

Figure A2- 1Thermograms obtained from IR thermography for 800N

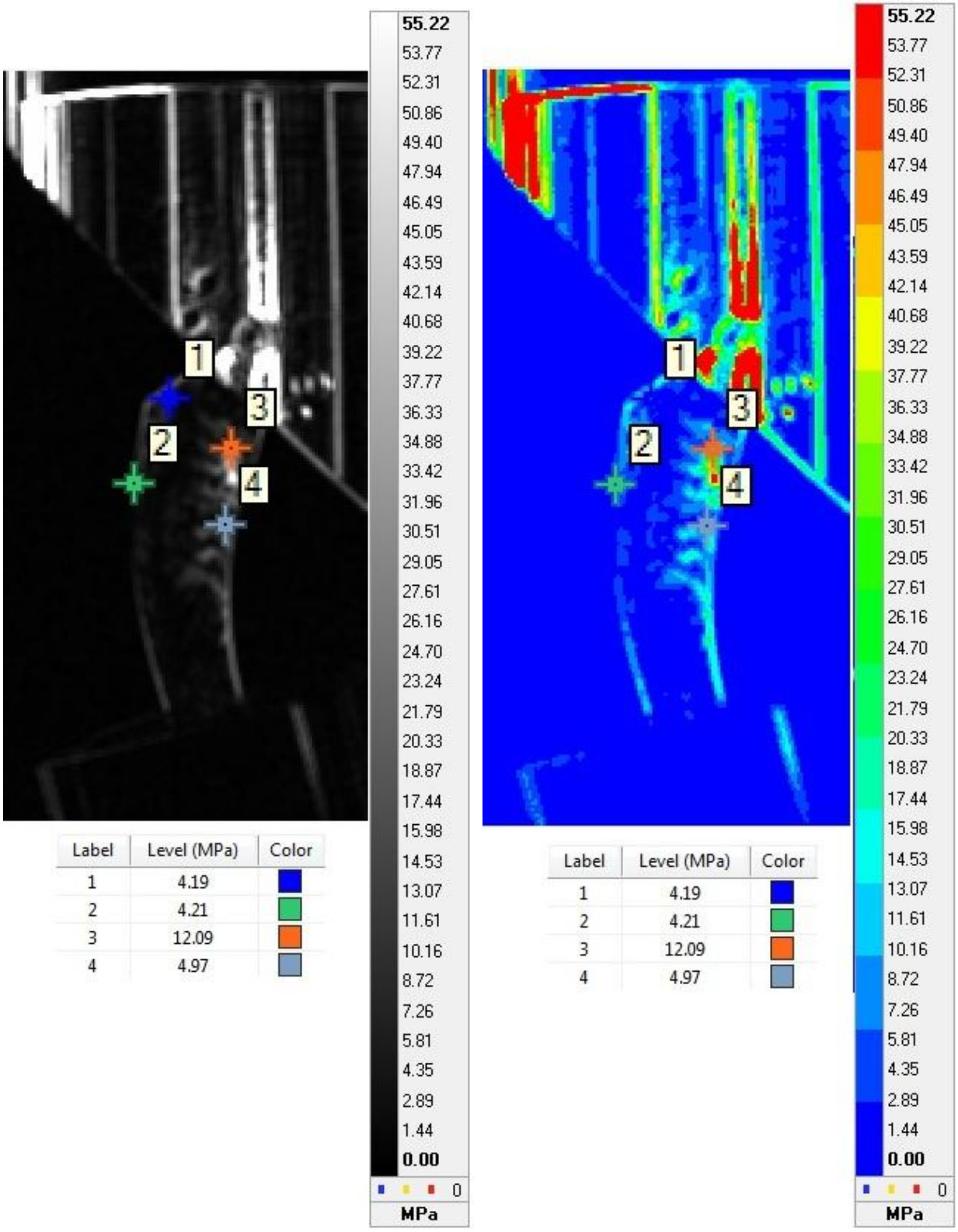

Figure A2- 2Thermograms obtained from IR thermography for 1400N

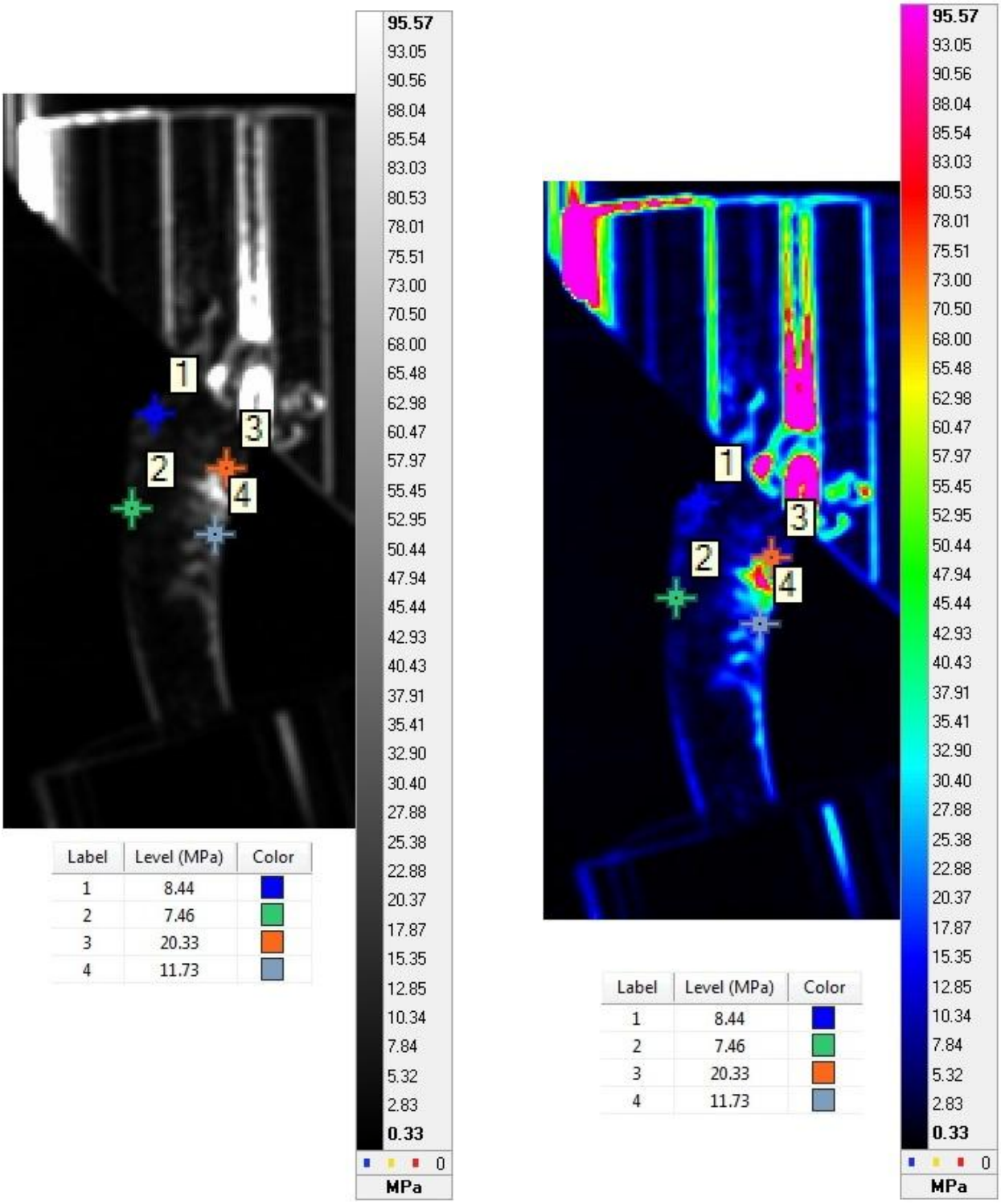

Figure A2- 3Thermograms obtained from IR thermography for 2200N

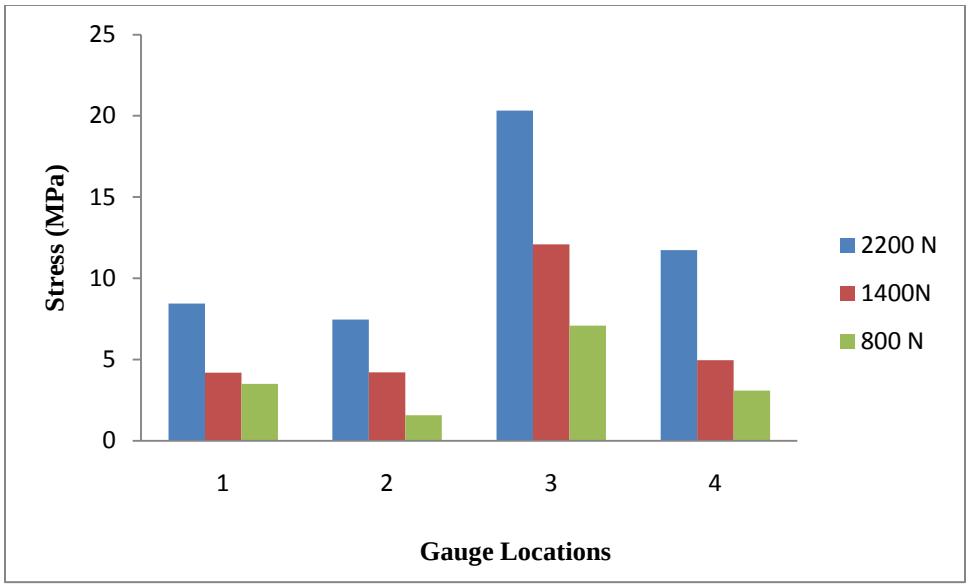

Figure A2- 4 Bar chart of stress values obtained from IR thermography

APPENDIX 3: Comparison of Strain values from FEA and Strain Gauge Experiments

Strain			
Vertex	FE Model (με)	Strain gauge (με)	%
1	133	190	30
2	199	200	0.5
3	682	580	-17.59
4	785	220	-256.82

$$\%Difference = \frac{(Experimental\ Strain - FEA\ Strain)}{Experimental\ Strain} \times 100$$

Table A3- 1 Comparison of strain gauge and FE strains for 800N.

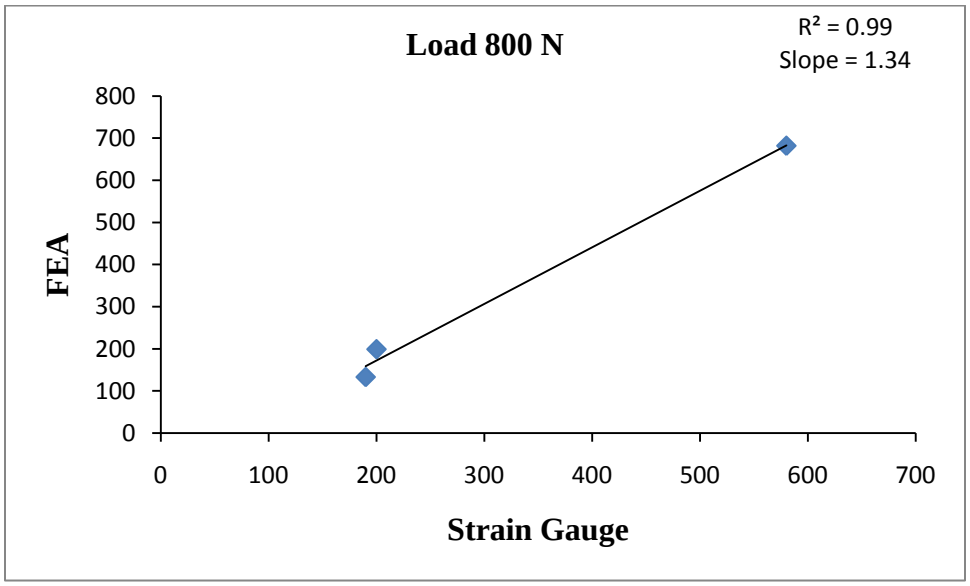

Figure A3- 1 Correlation graph of strain gauge and FE strains for 800N, excluding vertex 4.

Strain			
Vertex	FE Model (με)	Strain gauge (με)	%
1	226	275	17.82
2	345	275	-25.45
3	1216	800	-52
4	1372	325	-322.15

$$\%Difference = \frac{(Experimental\ Strain - FEA\ Strain)}{Experimental\ Strain} \times 100$$

Table A3- 2 Comparison of strain gauge and FE strains for 1400N.

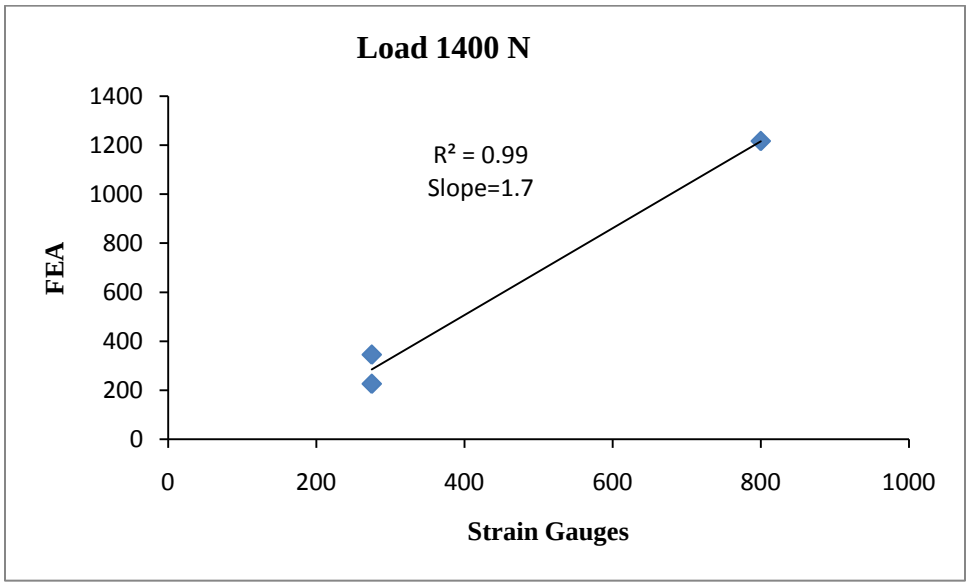

Figure A3- 2 Correlation graph of strain gauge and FE strains for 1400N, excluding vertex 4.

Strain			
Vertex	FE Model (με)	Strain gauge (με)	%
1	361	450	19.78
2	540	475	-13.68
3	1840	1400	-31.43
4	2172	520	-317.69

$$\%Difference = \frac{(Experimental\ Strain - FEA\ Strain)}{Experimental\ Strain} \times 100$$

Table A3- 3 Comparison of strain gauge and FE strains for 2200N.

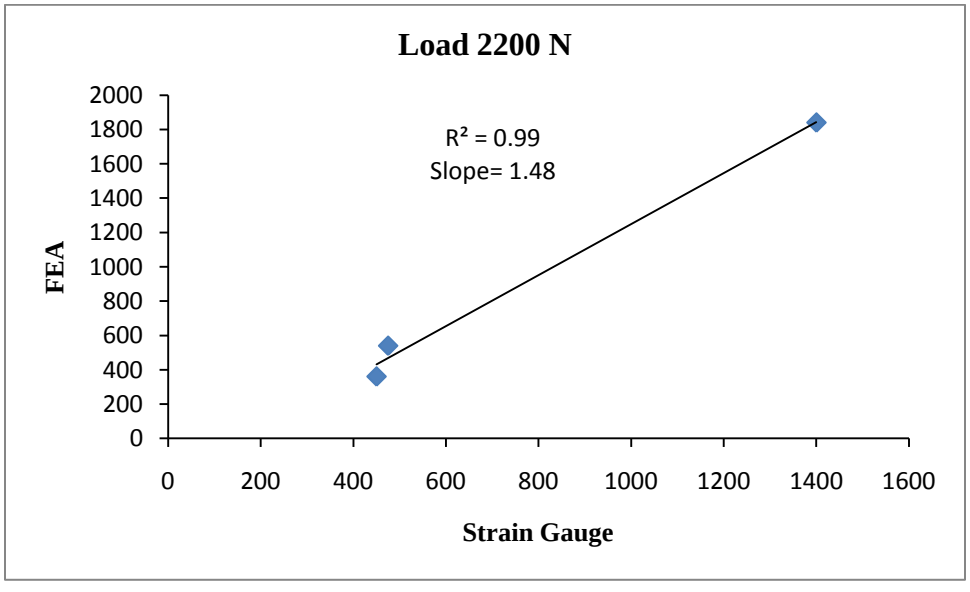

Figure A3- 3 Correlation graph of strain gauge and FE strains for 2200N, excluding vertex 4.

APPENDIX 4: Comparison of Stress values from IR and Strain Gauge Experiment

Stress			
Vertex	Reading from Strain gauge (MPa)	IR Stress (MPa)	%
1	2.76	3.5	-26.81
2	2.90	1.58	45.52
3	8.41	7.1	15.58
4	3.19	3.1	2.82

$$\%Difference = \frac{(Strain\,Gauge\,Stress - IR\,Stress)}{Strain\,Gauge} \times 100$$

Table A4- 1 Comparison of strain gauge and IR stress for 800N

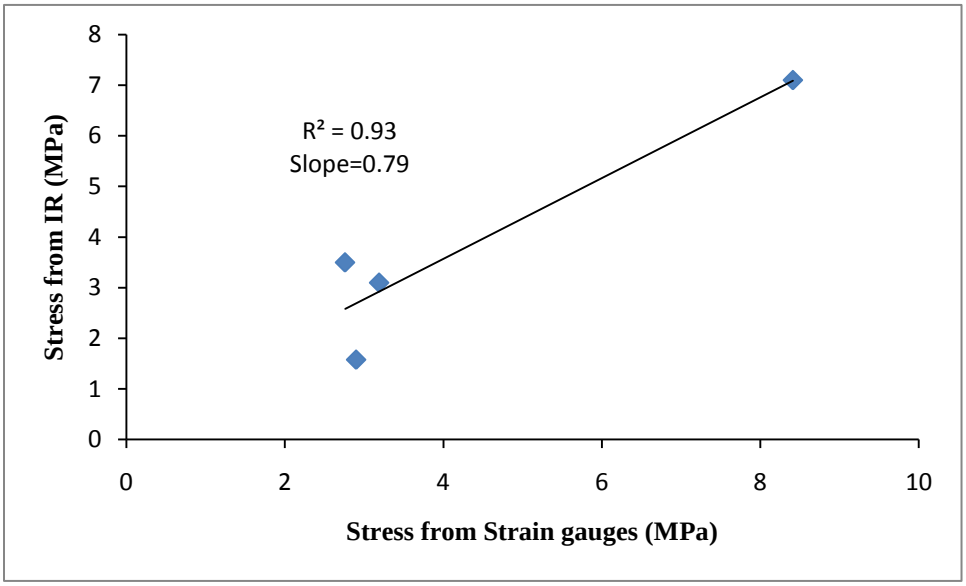

Figure A4- 1 Correlation graph of strain gauge and IR stress for 800N.

There is little or no 'offset' in stress due to preload in this comparison, since IR and strain gauge tests used the same preload.

Stress			
Vertex	Reading from Strain gauge (MPa)	IR Stress (MPa)	%
1	3.99	4.19	-5.01
2	3.99	4.21	-5.51
3	11.60	12.09	-4.22
4	4.71	4.97	-5.52

$$\%Difference = \frac{(Strain\,Gauge\,Stress - IR\,Stress)}{Strain\,Gauge} \times 100$$

Table A4- 2 Comparison of strain gauge and IR stress for 1400N

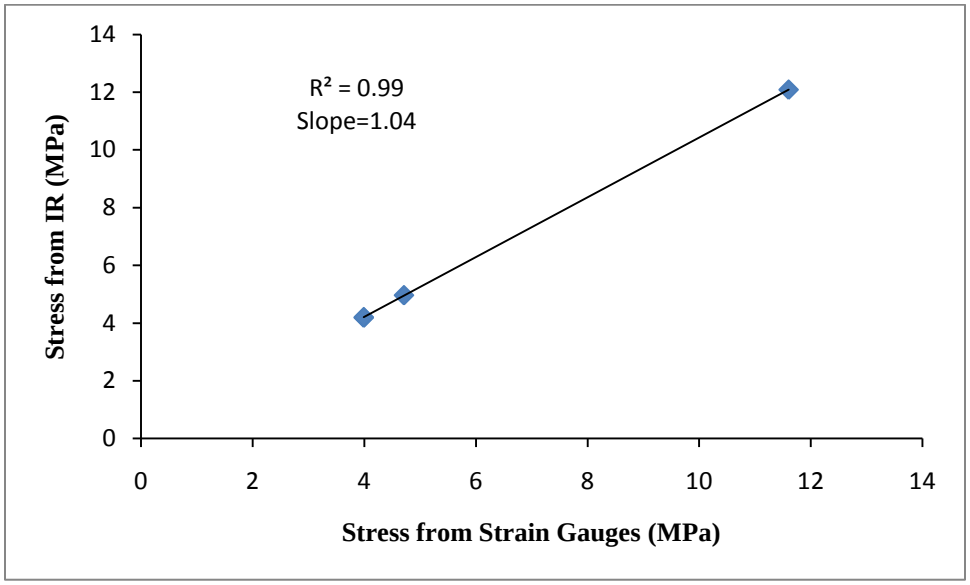

Figure A4- 2 Correlation graph of strain gauge and IR stress for 1400N.

There is a negligible 'offset' in stress due to preload in this comparison, since IR and strain gauge tests used the same preload.

Stress			
Vertex	Reading from Strain gauge (MPa)	IR Stress (MPa)	%
1	6.53	8.44	-29.25
2	6.89	7.46	-8.27
3	20.30	20.33	-0.15
4	7.54	11.73	-55.57

$$\%Difference = \frac{(Strain\,Gauge\,Stress - IR\,Stress)}{Strain\,Gauge} \times 100$$

Table A4- 3 Comparison of strain gauge and IR stress for 2200N

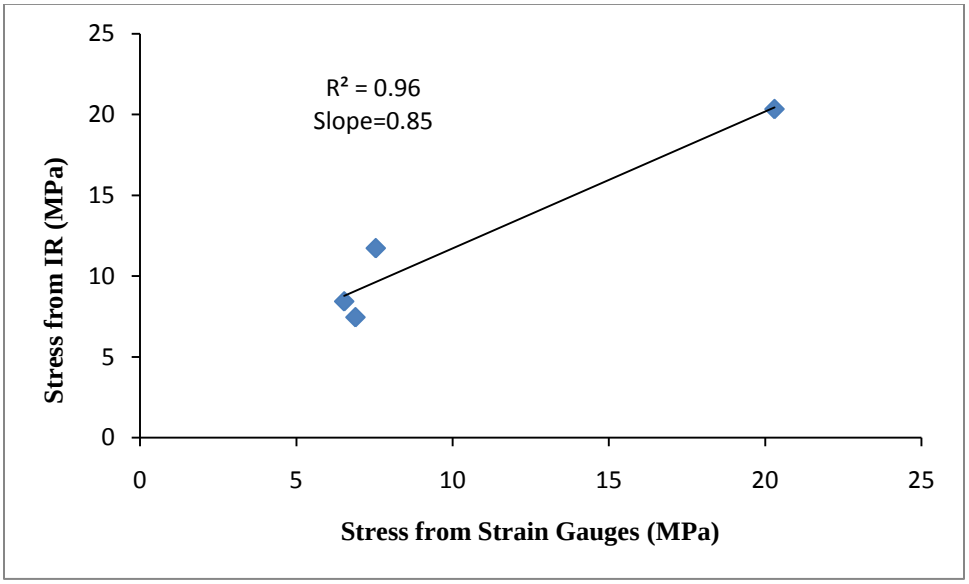

Figure A4- 3 Correlation graph of strain gauge and IR stress for 2200N.

There is only a small 'offset' in stress due to preload in this comparison, since IR and strain gauge tests used the same preload.

APPENDIX 5: Load vs Displacement graphs for all three applied loads

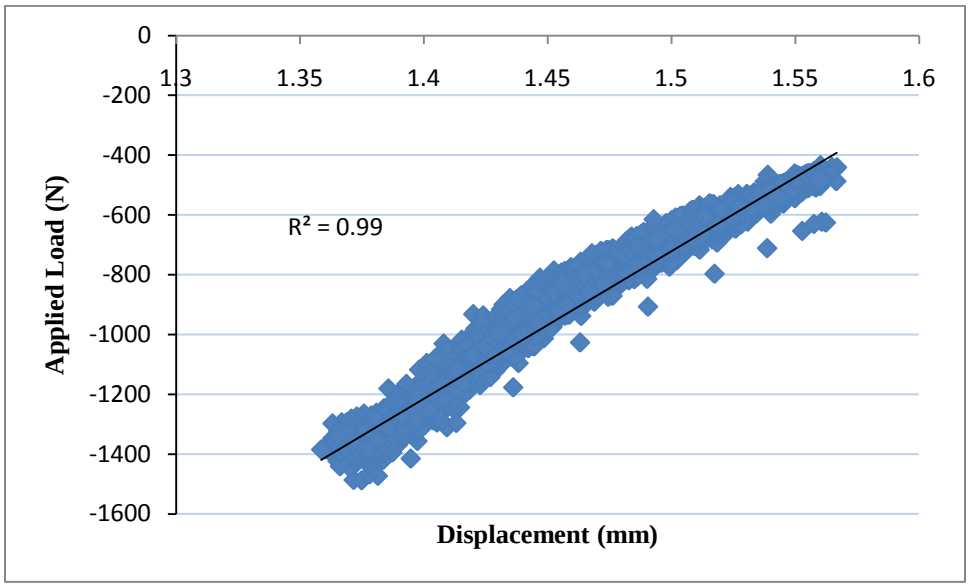

Figure A5- 1 Load-displacement graph for 800N (average)

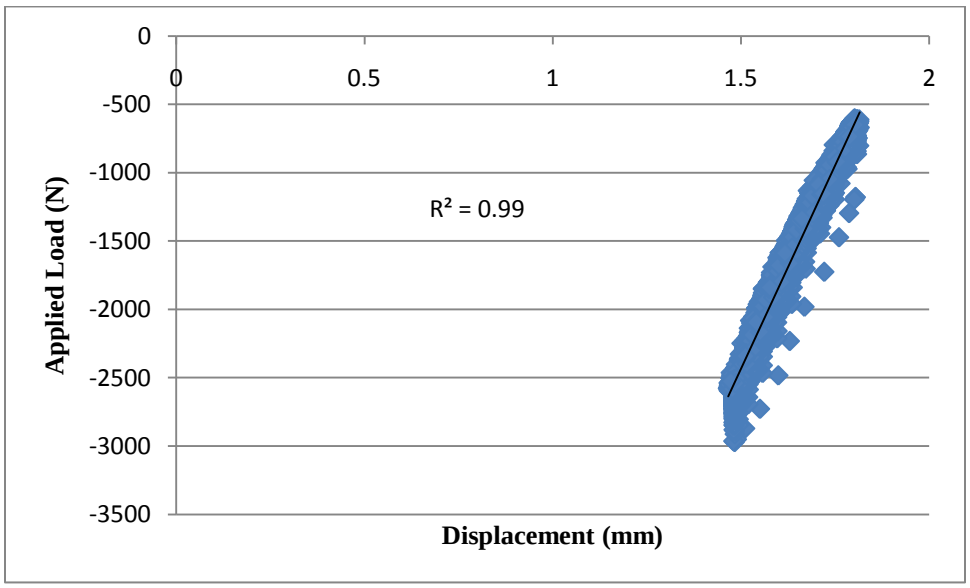

Figure A5- 2 Load-displacement graph for 1400N (average)

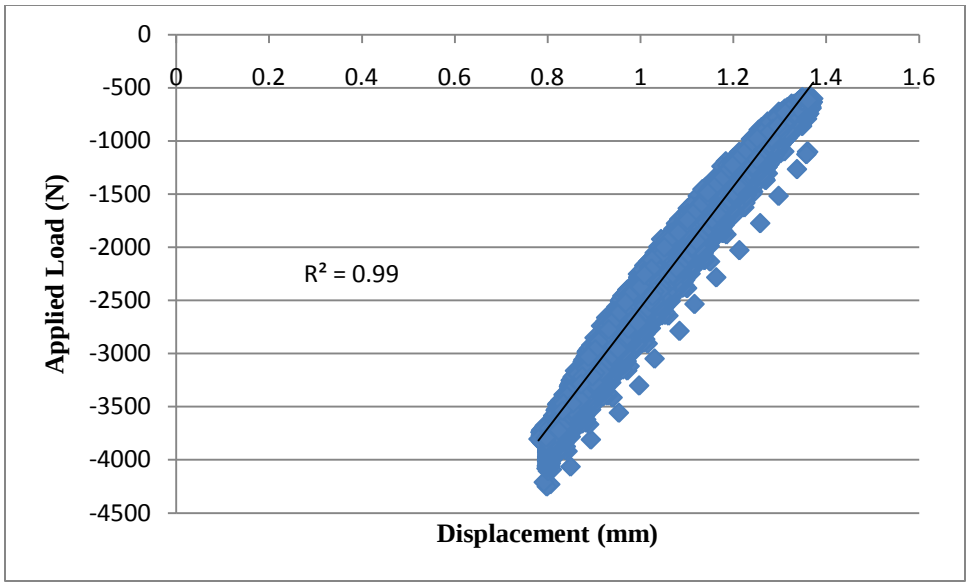

Figure A5- 3 Load-displacement graph for 2200N (average)

REFERENCES

[1] Kurtz, S.M., Lau, E., Ong, K., Zhao, K., Kelly, M., Bozic, K.J. Future young patient demand for primary and revision joint replacement: National projections from 2010 to 2030. Clinical Orthopaedics and Related Research 2009; 467 (10): 2606-2612

[2] Gross S, Abel EW. A finite element analysis of hollow stemmed hip prostheses as a means of reducing stress shielding of the femur. Journal of Biomechanics 2001; 34: 995-1003

[3] Sabatini AL, Goswami T. Hip implants VII: Finite element analysis and optimization of cross-sections. Materials and Design 2008; 29: 1438-1446

[4] Nantel J, Termoz N, Vendittoli P, Lavigne M, Prince F. Gait Patterns After Total Hip Arthroplasty and Surface Replacement Arthroplasty. Archives of Physical Medicine and Rehabilitation 2009; 90: 463-469

[5] Nantel J, Termoz N, Centomo H, Lavigne M, Vendittoli PA, Prince F. Postural balance during quiet standing in patients with total hip arthroplasty and surface replacement arthroplasty. Clinical Biomechanics 2008; 23: 402-407

[6] Berend KR, Lombardi AV, Mallory TH, Dodds KL, Adams JB. Cementless double-tapered total hip arthroplasty in patients 75 years of age and older. Journal of Arthroplasty 2004; 19: 288-295

[7] Wall JC, Ashburn A, Klenerman L. Gait analysis in the assessment of functional performance before and after total hip replacement. Journal of Biomedical Engineering 1981; 3: 121-127

[8] Bennett D, Goswami T. Finite element analysis of hip stem designs. Materials and Design 2008; 29: 45-60

[9] Raj K. Sinha, ed. Hip Replacement : Current Trends and Controversies. USA: Marcel Dekker, Inc. 270 Madison Avenue, New York, NY 10016. 2002

[10] Dictionary. http://encarta.msn.com/encnet/features/dictionary/dictionaryhome.aspx; 2009

[11] Ramakrishna S, Mayer J, Wintermantel E, Leong KW. Biomedical applications of polymer-composite materials: A review. Composites Science and Technology 2001; 61: 1189-1224

[12] Lewandowska-Szumie M, Komender J, Chopek J. Interaction between carbon composites and bone after intrabone implantation. Journal of Biomedical Materials Research 1999; 48: 289-296

[13] Reddy JN, Chao WC. Finite-element analysis of laminated bimodulus composite-material plates. Computers and Structures 1980; 12: 245-251

[14] Dimitrievska S, Whitfield J, Hacking SA, Bureau MN. Novel carbon fiber composite for hip replacement with improved in vitro and in vivo osseointegration. Journal of Biomedical Materials Research - Part A 2009; 91: 37-51

[15] Bauer DC, Hunter DJ, Abramson SB, Attur M, Corr M, Felson D, Heinegard D, Jordan JM, Kepler TB, Lane NE, Saxne T, Tyree B, Kraus VB, For the Osteoarthritis Biomarkers Network (V. Kraus,Chair). Classification of osteoarthritis biomarkers: a proposed approach. Osteoarthritis and Cartilage 2006; 14: 723-727

[16] Ganz DA, Chang JT, Roth CP, Guan M, Kamberg CJ, Niu F, Reuben DB, Shekelle PG, Wenger NS, Maclean CH. Quality of osteoarthritis care for community-dwelling older adults. Arthritis & Rheumatism 2006; 55: 241-247

[17] Reilly K, Barker K, Shamley D, Newman M, Oskrochi GR, Sandall S. The role of foot and ankle assessment of patients with lower limb osteoarthritis. Physiotherapy 2009; 95: 164-169

[18] Canadian Institute for Health Information. Hip and Knee Replacements in Canada-Canadian Joint Replacement Registry (CJRR) 2008-2009 Annual Report 2009: 1-89

[19] Bouziane MM, Bachir Bouiadjra B, Benbarek S, Tabeti MSH, Achour T. Finite element analysis of the behaviour of microvoids in the cement mantle of cemented hip stem: Static and dynamic analysis. Materials and Design 2010; 31: 545-550

[20] Bozic KJ, Saleh KJ, Rosenberg AG, Rubash HE. Economic evaluation in total hip arthroplasty. Journal of Arthroplasty 2004; 19: 180-189

[21] Katoozian H, Davy DT, Arshi A, Saadati U. Material optimization of femoral component of total hip prosthesis using fiber reinforced polymeric composites. Medical Engineering and Physics 2001; 23: 505-511

[22] Wylde V, Blom AW, Whitehouse SL, Taylor AH, Pattison GT, Bannister GC. Patient-Reported Outcomes After Total Hip and Knee Arthroplasty. The Journal of arthroplasty 2009; 24: 210-216

[23] Siopack JS, Jergesen HE. Total hip arthroplasty. Western Journal of Medicine 1995; 162: 243-249

[24] Kuhlman G, Domb B. Hip Impingement: Identifying and Treating a Common Cause of Hip Pain. American Family Physician 2009; 80: 1429

[25] Pluot E, Davis ET, Revell M, Davies AM, James SLJ. Hip arthroplasty. Part 1: prosthesis terminology and classification. Clinical radiology 2009; 64: 954-960

[26] Rahaman MN, Yao A, Bal BS, Garino JP, Ries MD. Ceramics for Prosthetic Hip and Knee Joint Replacement. Journal of the American Ceramic Society 2007; 90: 1965-1988

[27] Berger RA, Seel MJ, Wood K, Evans R, D'Antonio J, Rubash HE. Effect of a centralizing device on cement mantle deficiencies and initial prosthetic alignment in total hip arthroplasty. Journal of Arthroplasty 1997; 12: 434-443

[28] Maillefert JF, Roy C, Cadet C, Nizard R, Berdah L, Ravaud P. Factors influencing surgeons' decisions in the indication for total joint replacement in hip osteoarthritis in real life. Arthritis & Rheumatism 2008; 59: 255-262

[29] Quintana JM, Aróstegui I, Azkarate J, Goenaga JI, Elexpe X, Letona J, Arcelay A. Evaluation of explicit criteria for total hip joint replacement. Journal of clinical epidemiology 2000; 53: 1200-1208

[30] Quintana JM, Aróstegui I, Azkarate J, Goenaga JI, Tobio R, Aranburu JM, Goikoetxea B. Use of explicit criteria for total hip joint replacement fixation techniques. Health Policy 2002; 60: 1-16

[31] Diulus CA, Krebs VE, Hanna G, Barsoum WK. Hip Arthroscopy. The Journal of arthroplasty 2006; 21: 68-73

[32] Altman RD, Abadie E, Avouac B, Bouvenot G, Branco J, Bruyere O, Calvo G, Devogelaer J-, Dreiser RL, Herrero-Beaumont G, Kahan A, Kreutz G, Laslop A, Lemmel EM, Menkes CJ, Pavelka K, Van De Putte L, Vanhaelst L, Reginster J-. Total joint replacement of hip or knee as an outcome measure for structure modifying trials in osteoarthritis. Osteoarthritis and Cartilage 2005; 13: 13-19

[33] Ingham E, Fisher J. Biological reactions to wear debris in total joint replacement. Proceedings of the Institution of Mechanical Engineers 2000; 214: 21-37

[34] Bartel DL, Bicknell VL, Wright TM. The effect of conformity, thickness, and material on stresses in ultra-high molecular weight components for total joint replacement. Journal of Bone and Joint Surgery 1987; 69: 471-474

[35] Gladius L. Contact stress at articular surfaces in total joint replacements. Part I: Experimental methods. Biomedical Materials and Engineering 1998; 8: 91

[36] Wang A, Lin R, Stark C, Dumbleton JH. Suitability and limitations of carbon fiber reinforced PEEK composites as bearing surfaces for total joint replacements. Wear 1999; 225-229: 724-727

[37] Cheung H, Ho M, Lau K, Cardona F, Hui D. Natural fibre-reinforced composites for bioengineering and environmental engineering applications. Composites Part B 2009; 40: 655-663

[38] Chen H, Morrey BF, An K, Luo Z. Bone Remodeling Characteristics of a Short-Stemmed Total Hip Replacement. The Journal of arthroplasty 2009; 24: 945-950

[39] Mano JF, Sousa RA, Boesel LF, Neves NM, Reis RL. Bioinert, biodegradable and injectable polymeric matrix composites for hard tissue replacement: state of the art and recent developments. Composites Science and Technology 2004; 64: 789-817

[40] Kaddick C, Stur S, Hipp E. Mechanical simulation of composite hip stems. Medical engineering & physics 1997; 19: 431-439

[41] Campbell M, Bureau MN, Yahia L. Performance of CF/PA12 composite femoral stems. Journal of Materials Science: Materials in Medicine 2008; 19: 683-693

[42] Campbell M, Denault J, Yahia L, Bureau MN. CF/PA12 composite femoral stems: Manufacturing and properties. Composites Part A 2008; 39: 796-804

[43] Campbell M, Bureau MN, Bougherara HA, Denault J, Yahia LH. Biomimetic polymer composites for orthopedic implants. Annual Technical Conference - ANTEC, Conference Proceedings 2006; 1: 158-162

[44] Campbell M, Bougherara HA, Yahia L, Bureau MN, Legoux J-, Denault J. Biomimetic polymer composites for orthopedic hip implants. Medical Device Materials III - Proceedings of the Materials and Processes for Medical Devices Conference 2005 2006; 2006: 49-54

[45] Bougherara H, Bureau M, Campbell M, Vadean A, Yahia L. Design of a biomimetic polymer-composite hip prosthesis. Journal of Biomedical Materials Research Part A 2007; 82A: 27-40

[46] Snyder SM, Schneider E. Estimation of mechanical properties of cortical bone by computed tomography. Journal of Orthopaedic Research 1991; 9: 422-431

[47] Campbell M, Bureau MN, Yahia L. Performance of CF/PA12 composite femoral stems. Journal of Materials Science: Materials in Medicine 2008; 19: 683-693

[48] Kurokawa M, Uchiyama Y, Iwai T, Nagai S. Performance of plastic gear made of carbon fiber reinforced polyamide 12. Wear 2003; 254: 468-473

[49] Mahboob Z. Validated Finite Element Study of Stress Shielding in a Novel Hybrid Knee Implant 2009: 1-145

[50] Doudard C, Calloch S, Hild F, Roux S. Identification of heat source fields from infrared thermography: Determination of 'self-heating' in a dual-phase steel by using a dog bone sample. Mechanics of Materials 2010; 42: 55-62

[51] Raso AM, Raso SM. Correlations between angiography and thermography using liquid crystals on a plate in Raynaud syndrome. Minerva medica 1975; 66: 3985-3989

[52] Niechajev IA, Lindell SE, Karlsson S. Angiography, thermography and other circulation tests in vascular tumours of the hand. Vascular surgery 1983; 17: 226-239

[53] Miland AO, De Weerd L, Mercer JB. Intraoperative use of dynamic infrared thermography and indocyanine green fluorescence video angiography to predict partial skin flap loss. European Journal of Plastic Surgery 2008; 30: 269-276

[54] Okada Y, Kawamata T, Kawashima A, Hori T. Intraoperative application of thermography in extracranial-intracranial bypass surgery. Neurosurgery 2007; 60: ONS-362-ONS-365

[55] Kaczmarek M, Nowakowski A, Siebert J, Rogowski J. Infrared thermography - applications in heart surgery. Proceedings of SPIE - The International Society for Optical Engineering 1999; 3730: 184-188

[56] Wishart GC, Campisi M, Boswell M, Chapman D, Shackleton V, Iddles S, Hallett A, Britton PD. The accuracy of digital infrared imaging for breast cancer detection in women undergoing breast biopsy. European Journal of Surgical Oncology 2010; 36: 535-540

[57] Arora N, Martins D, Ruggerio D, Tousimis E, Swistel AJ, Osborne MP, Simmons RM. Effectiveness of a noninvasive digital infrared thermal imaging system in the detection of breast cancer. American Journal of Surgery 2008; 196: 523-526

[58] Umadevi V, Suresh S, Raghavan SV. Improved infrared thermography based image construction for biomedical applications using Markov Chain Monte Carlo method.Conference proceedings: Annual International Conference of the IEEE Engineering in Medicine and Biology Society.IEEE Engineering in Medicine and Biology Society.Conference 2009; 2009: 5360-5363

[59] Sauer H. Infrared thermography for the prevention and early detection of breast cancer. KIM - Komplementare und Integrative Medizin, Artztezeitschrift fur Naturheilverfahren 2008; 49: 29-33

[60] Kapoor P, Prasad SVAV. Image processing for early diagnosis of breast cancer using infrared images. 2010 The 2nd International Conference on Computer and Automation Engineering, ICCAE 2010 2010; 3: 564-566

[61] Jiang L, Zhan W, Loew MH. A numerical study of the inverse problem of breast infrared thermography modeling. Progress in Biomedical Optics and Imaging - Proceedings of SPIE 2010; 7626

[62] Boquete L, Ortega S, Miguel-Jiménez JM, Rodríguez-Ascariz JM, Blanco R. Automated Detection of Breast Cancer in Thermal Infrared Images, Based on Independent Component Analysis. Journal of medical systems 2010: 1-9

[63] Baltag O, Banarescu A, Costandache D, Rau M, Ojica S. Microwaves and infrared thermography - Applications in early breast cancer detection. IFMBE Proceedings 2009; 26 IFMBE: 195-198

[64] Benington IC, Biagioni PA, Crossey PJ, Hussey DL, Sheridan S, Lamey P-. Temperature changes in bovine mandibular bone during implant site preparation: An assessment using infra-red thermography. Journal of dentistry 1996; 24: 263-267

[65] Watanabe F, Tawada Y, Komatsu S, Hata Y. Heat distribution in bone during preparation of implant sites: heat analysis by real-time thermography.. The International journal of oral & maxillofacial implants 1992; 7: 212-219

[66] Nam O, Yu W, Choi MY, Kyung H-. Monitoring of bone temperature during osseous preparation for orthodontic micro-screw implants: Effect of motor speed and ressure. Key Engineering Materials 2006; 321-323 II: 1044-1047

[67] Watanabe F, Tawada Y, Komatsu S, Hata Y. Heat distribution within the bone tissue by rotary cutting instrument for IMZ implant. Heat analysis by a real-time thermography. Nippon Hotetsu Shika Gakkai zasshi 1990; 34: 18-24

[68] Ishizaki NT, Matsumoto K, Kimura Y, Wang X, Kinoshita J-, Okano SM, Jayawardena JA. Thermographical and morphological studies of Er,Cr:YSGG laser irradiation on root canal walls. Photomedicine and Laser Surgery 2004; 22: 291-297

[69] Kreisler M, Schoof J, Langnau E, Al Haj H, d'Hoedt B. Temperature elevations in endosseous dental implants and the peri-implant bone during diode-laser-assisted surface decontamination. Proceedings of SPIE - The International Society for Optical Engineering 2002; 4610: 21-30

[70] Pawar S, Peters K. Transient infrared thermography for damage evaluation in aerospace composites. Proceedings of SPIE - The International Society for Optical Engineering 2010; 7649

[71] Dragan K, Swiderski W. Studying efficiency of NDE techniques applied to composite materials in aerospace applications. Acta Physica Polonica A 2010; 117: 878-883

[72] Findeis D, Gryzagoridis J, Musonda V. NDT detection and quantification of induced defects on composite helicopter rotor blade and UAV wing sections. Proceedings of SPIE - The International Society for Optical Engineering 2008; 7155

[73] Gryzagoridis J, Findeis D. Simultaneous shearographic and thermographic NDT of aerospace materials. Insight: Non-Destructive Testing and Condition Monitoring 2006; 48: 294-297

[74] Servais P, Gerlach N, Habermehl J, Ibarra-Castanedo C, Maldague X. Characterization of manufacturing and maintenance of aerospace composite discontinuities using infrared thermography. Materials Evaluation 2008; 66: 955-962

[75] Huang S, Li L, Yang H, Shi K. NDE of composites delamination by infrared thermography. Proceedings of SPIE - The International Society for Optical Engineering 2003; 5046: 219-223

[76] Halabe UB, Vasudevan A, Klinkhachorn P, Gangarao HVS. Detection of subsurface defects in fiber reinforced polymer composite bridge decks using digital infrared thermography. Nondestructive Testing and Evaluation 2007; 22: 155-175

[77] Meola C, Carlomagno GM, Giorleo L. Geometrical Limitations to Detection of Defects in Composites by Means of Infrared Thermography. Journal of Nondestructive Evaluation 2004; 23: 125-132

[78] Meola C, Carlomagno GM, Squillace A, Prisco U, Morace RE. Analysis of composites with infrared thermography. Macromolecular Symposia 2005; 228: 273-286

[79] Zhao Y, Guo X, Ren M, Wang X, He Y. Lock-in thermography method for the NDT of composite materials. Proceedings of SPIE - The International Society for Optical Engineering 2009; 7375

[80] Miller R, Chu TP, Filip P, Don J. Detection of defects in C/C composites using infrared thermography. Society for Experimental Mechanics - 11th International Congress and Exhibition on Experimental and Applied Mechanics 2008 2008; 3: 1245-1252

[81] Titman DJ. Applications of thermography in non-destructive testing of structures. NDT and E International 2001; 34: 149-154

[82] Swiderski W. Lock-in Thermography to rapid evaluation of destruction area in composite materials used in military applications. Sixth International Conference on Quality Control by Artificial Vision 2003; 5132

[83] Escourbiac F, Constans S, Courtois X, Durocher A. Application of lock-in thermography non destructive technique to CFC armoured plasma facing components. Journal of Nuclear Materials 2007; 367-370 B: 1492-1496

[84] Ghosh, K.K. and Karbhari, V.M. A critical review of infrared thermography as a method for non-destructive evaluation of FRP rehabilitated structures. Int. J. Materials and Product Technology 2006; 25: 241-266

[85] Liu J, Dai J, Wang Y. Research on lock in thermography for aerospace materials of nondestructive test based on image sequence processing. Proceedings of SPIE - The International Society for Optical Engineering 2009; 7375

[86] McLaughlin, P.V., McAssey, E.V. and Dietrich, R.C. Non-destructive examination of fibre composite structures by thermal field techniques. NDT&E International 1980; 13: 56-62

[87] McLaughlin VJ. Defect detection and quantification in laminated composites by EATF (passive) thermography. Review of Progress in Quantitative Nondestructive Evaluation 1988; 7B: 1125-1132

[88] Ball RJ, Almond DP. The detection and measurement of impact damage in thick carbon fibre reinforced laminates by transient thermography. NDT & E International 1998; 31: 165-173

[89] Wang Z, Liu J, Dai J. Lock-in thermography for evaluation of destruction area and determination of depth. Proceedings of SPIE - The International Society for Optical Engineering 2007; 6723

[90] Bai W, Wong BS. Evaluation of defects in composite plates under convective environments using lock-in thermography. Measurement Science and Technology 2001; 12: 142-150

[91] Ibarra-Castanedo C, Piau JM, Guilbert S, Avdelidis NP, Genest M, Bendada A, Maldague XPV. Comparative Study of Active Thermography Techniques for the Nondestructive Evaluation of Honeycomb Structures. Research in Nondestructive Evaluation 2009; 20: 1-31

[92] Maldague X. Nondestructive evaluation of materials by infrared thermography. Springer-Verlag 1993

[93] Maldague, X. and Marinetti, S. Pulse phase infrared thermography. Journal of Applied Physics 1996; 79: 2694-2698

[94] Bai, W., Wong, B.S.,. Non-destructive Evaluation of Aircraft Structure Using Lock-in Thermography. Nondestructive Evaluation of Aging Aircraft, Airports, and Aerospace Hardware IV, 2000; 3994

[95] Jones CH. Medical Thermography. IEEE proceedings. A, Physical science, measurement and instrumentation, management and education, reviews 1987; 134: 225-236

[96] Kaczmarek M, Nowakowski A, Siebert J, Rogowski J, Nowakowski A, Chachulski B. Infrared thermography: applications in heart surgery. SPIE 1999; 3730: 184-188

[97] Schaefer G, Závišek M, Nakashima T. Thermography based breast cancer analysis using statistical features and fuzzy classification. Pattern Recognition 2009; 42: 1133-1137

[98] Giansanti D. Improving spatial resolution in skin-contact thermography: Comparison between a spline based and linear interpolation. Medical Engineering and Physics 2008; 30: 733-738

[99] Allcock S, Ali MA. Early failure of a carbon-fiber composite femoral component. Journal of Arthroplasty 1997; 12: 356-358

[100] Mattila RH, Laurila P, Rekola J, Gunn J, Lassila LVJ, Mäntylä T, Aho AJ, Vallittu PK. Bone attachment to glass-fibre-reinforced composite implant with porous surface. Acta Biomaterialia 2009; 5: 1639-1646

[101] Fujihara K, Teo K, Gopal R, Loh PL, Ganesh VK, Ramakrishna S, Foong KWC, Chew CL. Fibrous composite materials in dentistry and orthopaedics: review and applications. Composites Science and Technology 2004; 64: 775-788

[102]Vishay Micro-Measurements. Strain Gage Selection: Criteria, Procedures, Recommendations Available at http://www.vishay.com/docs/11055/tn505.pdf 2007; 2010: 16

[103] Vishay Micro-Measurements. General Purpose Strain Gages – Linear Pattern Available at http://www.vishay.com/docs/11241/125uw.pdf 2009; 2010: 2

[104] National Instruments. Choosing the Right Strain-Gauge for Your Application Available at http://zone.ni.com/devzone/cda/tut/p/id/3092 2006; 2010

[105] Szivek JA, Gharpuray VM. Strain gauge measurements from bone surfaces. In: An YH, Draughn RA, eds. Mechanical Testing of Bone and the Bone-Implant Interface. Boca Raton, FL: CRC Press. 2000: 305-320

[106] Vishay Micro-Measurements. Surface Preparation for Strain Gage Bonding Available at http://www.vishay.com/docs/11129/11129_b1.pdf 2009; 2010: 7

[107] Illinois Tool Works. Table Model Axial Torsion: FastTrack™ 8874, Instron® Materials Testing Solutions (Instron.Us) Available at http://www.Instron.us/wa/products/fatigue_testing/table_axial_torsion.Aspx 2010; 2010

[108] Illinois Tool Works. Single Axis 8800 Series: Front Panel and FastTrack™ Console, Instron® Materials Testing Solutions (Instron.Us) Available at http://www.Instron.com/wa/library/StreamFile.Aspx?doc=1191 2010; 2010

[109] Prendergast PJ. Finite element models in tissue mechanics and orthopaedic implant design. Clinical Biomechanics 1997; 12: 343-366

[110] Cedip Infrared Systems. SILVER User Manual. SILVER User Manual: 1-23

[111] Rohlmann A, Mössner U, Bergmann G, Kölbel R. Finite-element-analysis and experimental investigation in a femur with hip endoprosthesis. Journal of Biomechanics 1983; 16: 727-742

[112] Viceconti M, Baleani M, De Lollis A, Toni A. An FEA-based protocol for the pre-clinical validation of custom-made hip implants. Journal of Medical Engineering and Technology 1998; 22: 257-262

[113] Helgason B, Pálsson H, Rúnarsson TP, Frossard L, Viceconti M. Risk of failure during gait for direct skeletal attachment of a femoral prosthesis: A finite element study. Medical Engineering and Physics 2009; 31: 595-600

[114] Khursheed S. A biomechanical study of a novel biomimetic hip implant 2009: 1-116

[115] Akay M, Aslan N. Numerical and experimental stress analysis of a polymeric composite hip joint prosthesis. Journal of Biomedical Materials Research 1996; 31: 167-182

[116] Otani T, Whiteside LA, White SE. Strain distribution in the proximal femur with flexible composite and metallic femoral components under axial and torsional loads. Journal of Biomedical Materials Research 1993; 27: 575-585

[117] O'Connor DO, Burke DW, Jasty M, Sedlacek RC, Harris WH. In vitro measurement of strain in the bone cement surrounding the femoral component of total hip replacements during simulated gait and stair-climbing. Journal of Orthopaedic Research 1996; 14: 769-777

[118] Simões JA, Vaz MA. The influence on strain shielding of material stiffness of press-fit femoral components. Proceedings of the Institution of Mechanical Engineers, Part H: Journal of Engineering in Medicine 2002; 216: 341-346

[119] Bougherara H, Zdero R, Shah S, Miric M, Papini M, Zalzal P, Schemitsch EH. A biomechanical assessment of modular and monoblock revision hip implants using FE analysis and strain gage measurements, J Orthopaedic Surgery and Research, 2010 May 12;5:34.

[120] El'Sheikh HF, MacDonald BJ, Hashmi MSJ. Finite element simulation of the hip joint during stumbling: a comparison between static and dynamic loading. J Mater Process Technol 2003;143-144:249-55.

[121]Bergmann G, Deuretzbacher G, Heller M, Graichen F, Rohlmann A, Strauss J, Duda GN. Hip contact forces and gait patterns from routine activities. Journal of Biomechanics 2001; 34: 859-871

[122] Bergmann G, Graichen F, Rohlmann A: Hip joint loading during walking and running, measure in two patients. J Biomech 1993, 26(8):969-990.